Convective hydration in the tropical tropopause layer during the StratoClim aircraft campaign: Pathway of an observed hydration patch

Keun-Ok Lee[1], Thibaut Dauhut[1], Jean-Pierre Chaboureau[1], Sergey Khaykin[2], Martina Krämer[3] and Christian Rolf[3]

[1]Laboratoire d'Aérologie, Université de Toulouse, CNRS, UPS, Toulouse, France

[2] LATMOS-IPSL, Universié Versailles St-Quentin; Sorbonne Université, CNRS/INSU, Guyancourt, France

[3]Institute for Energy and Climate Research – Stratosphere (IEK-7), Forschungzentrum Jülich, Jülich, Germany

ABSTRACT

The source and pathway of the hydration patch in the TTL (Tropical Tropopause Layer) that was measured during the StratoClim field campaign during the Asian summer monsoon in 2017, and its connection to convective overshoots are investigated. During flight #7, two remarkable layers are measured in the TTL namely, (1) moist layer (ML) with water vapour content of 4.8−5.7 ppmv in altitudes of 18−19 km altitudes in the lower stratosphere, and (2) ice layer (IL) with ice content up to 1.9 eq. ppmv in altitudes of 17−18 km in the upper troposphere around 06:30 UTC on 8 August to the south of Kathmandu (Nepal). A Meso-NH convection-permitting simulation succeeds in reproducing the characteristics of ML and IL. Through analysis, we show that ML and IL are generated by convective overshoots that occurred over the Sichuan basin about 1.5 day before. Overshooting clouds develop up to 19 km, hydrating the lower stratosphere of up to 20 km with 6401 t of water vapour by a strong-to-moderate mixing of the updraughts with the stratospheric air. A few hours after the initial overshooting phase, a hydration patch is generated, and a large amount of water vapour (above 18 ppmv) remained at even higher altitudes up to 20.5 km while the anvil cloud top descends to 18.5 km. At the same time, a great part of the hydrometeors falls shortly, and the water vapour concentration in ML and IL decreases due to turbulent diffusion by mixing with the tropospheric air, ice nucleation, and water vapour deposition. As the hydration patch continues to travel toward the south of Kathmandu, tropospheric tracer concentration increases up to ~30 and 70 % in ML and IL, respectively. The air mass in the layers becomes gradually diffused and it has less and less water vapour and ice content by mixing with the dry tropospheric air.

1. Introduction

The Asian summer monsoon anticyclone is one of the most pronounced circulation patterns in the Northern Hemisphere, and it is a dominant climatological feature of the global circulation during boreal summer (Mason and Anderson, 1963; Randel and Park, 2006). The monsoon circulation horizontally covers large parts of southern Asia and the Middle East, and is located on the edge of the tropics and subtropics. It consists of cyclonic flow and convergence in the lower troposphere together with strong anticyclonic circulation and divergence in the upper troposphere. This circulation is coupled with persistent deep convection over the south Asia region during summer (June to September) (Hoskins and Rodwell, 1995). The monsoon tropopause is relatively high at about 4.2 ppmv; the upper tropospheric anticyclonic circulation extends into the lower stratosphere spanning from around 300 hPa and 70 hPa, i.e. approximately the whole upper troposphere and lower stratosphere (UTLS) (Highwood and Hoskins, 1998; Randel and Park, 2006).

Due to the strong dynamical signature in the UTLS, the influence of the monsoon is evident in chemical constituents, i.e. water vapour is relatively high at about 4.2 ppmv (Wright et al., 2011), ozone is relatively low (Randel et al., 2001), and methane, nitrogen oxides, and carbon monoxide are relatively high (Park et al., 2004; Liu et al., 2005). Especially, the water vapour in the UTLS is controlled by the troposphere-to-stratosphere transport of moisture across the tropical tropopause layer (TTL, located between ~150 hPa (355 K, 14 km) and ~70 hPa (425 K, 18.5 km); Fueglistaler et al., 2009; Rolf et al., 2018). It is mainly driven by the large-scale cold point tropopause temperature field, but also processes involving convection, gravity waves, and cirrus cloud microphysics that modulate TTL humidity.

Convective overshoots that penetrate the tropopause directly inject air and water into the stratosphere. Fundamentally, convection arises from the temperature difference between a parcel of warm air and the cooler air surrounding it. Warm air, which is less dense, i.e. more buoyant, rises through the atmospheric column and adiabatically expands and cools. When the temperature of the rising air parcel has cooled sufficiently, the water vapour it contains will begin to condense and release latent heat. If air parcels within the convective core have enough upward momentum, they continue to rise beyond their equilibrium level of zero buoyancy, and form overshoots. They eventually form an overshoot that penetrate into the lowermost stratosphere by crossing the cold point tropopause. The convective overshoots have the potential to increase

the humidity in the stratosphere via rapid sublimation of convectively lofted ice and mixing with dry stratospheric air. This has been demonstrated in previous studies in both modelling and measurement (Dessler and Sherwood, 2004; Chaboureau et al., 2007; Jensen et al., 2007; Homeyer et al., 2014; Khaykin et al., 2016; Rysman et al., 2016; Homeyer et al., 2017; Smith et al., 2017; Dauhut et al., 2018; Funatsu et al., 2018; among others). Even a small volume of tropospheric air can carry a significant quantity of water in the condensed phase. Mixing of tropospheric air with the surrounding stratosphere, which is typically sub-saturated, facilitates the rapid sublimation of lofted ice. Also, the origin of the injected water to the TTL has been studied by backward trajectory analysis at global scale, and it was found that the convective sources are generally higher over the continental part of the Asian monsoon region in comparison to other tropical regions, with shorter transit times (Tzella and Legras, 2005; Tissier and Legras, 2016). However, the net contribution of convective overshoots to stratospheric water vapour concentration is not well understood at mesoscale and is not well represented in global models because of the small spatial scales (less than a few kilometres) and short time sales (less than few hours) over which convection occurs.

The tropical aircraft campaign of the Stratospheric and upper tropospheric processes for better Climate predictions (StratoClim, www.stratoclim.org) took place in summer 2017. It aimed to improve our knowledge of the key processes, i.e. microphysical, chemical and dynamical processes, which determine the composition of the UTLS, such as the formation, loss, and redistribution of chemical constituents (water vapour, ozone, and aerosol). During the campaign, eight dedicated flights were successfully operated with the objective of documenting the connection between the moisture plumes in the UTLS and the convective sources from south Kathmandu, Nepal, during summer monsoon season.

Our study focuses on part of flight #7 to the south of Kathmandu measuring the stratospheric hydration in the altitudes between 17 and 19 km. The objective of our work is to investigate the source and pathway of the localized moisture in the TTL that was measured by aircraft in connection to a convective overshoot. This is done using a combination of airborne and spaceborne observations as well as a convection-permitting simulation performed with a fine resolution in the TTL.

A detailed description of the dataset is given in section 2. Section 3 presents the moistened TTL signature captured by airborne and spaceborne observations and the numerical simulation. Section 4 demonstrates the convective origin of the enhanced moisture and shows its evolution along its path in the lower stratosphere. A summary and discussion of the findings of the present study are given in section 5.

88

89

2. Data and method

M55-Geophysica aircraft deployment in Kathmandu during Asian Summer Monsoon in July-August 2017 provided unprecedented sampling of the UTLS region above the southern slopes of Himalayas. More details concerning the observational datasets used in this study together with the airborne and spaceborne measurements and the convection-permitting simulation are provided in the following.

2.1. StratoClim airborne observations

During flight #7, the M55-Geophysica aircraft flew back and forth between Kathmandu in Nepal and west Bengal in India (for the track, see the red line in Fig. 1) from 04:30 UTC to 06:50 UTC on 8 August 2017. In-situ sensor onboard the aircraft measures the relative humidity with respect to ice (hereafter called simply 'relative humidity' or 'RH$_{ice}$'), temperature and wind speed and direction every 1 second. FLASH and FISH instruments on board the Geophysica aircraft sampled the vertical water vapour and ice content distribution every 1 second, respectively.

FLASH-A (Fluorescent Lyman-Alpha Stratospheric Hygrometer for Aircraft) is an advanced version of the airborne FLASH instrument (Sitnikov et al, 2007; Khaykin et al., 2013) previously flown onboard the M55-Geophysica aircraft. FLASH-A has a rear facing inlet allowing measurement of gas-phase water in the altitude range between 12–21 km, with the latter being the aircraft ceiling altitude. Total uncertainty of water vapour measurement amounts to 9 % with a detection limit of 0.2 ppmv, whereas the measurement precision at 1 Hz sampling is better than 6 %.

FISH (Fast In situ Stratospheric Hygrometer) is a closed-path Lyman-α photo fragment fluorescence hygrometer that measures total water (sum of gas phase and evaporated ice crystals) in the range of 1–1000 ppmv between 50 and 500 hPa levels with an accuracy and precision of 6–8 % and 0.3 ppmv (Zöger et al., 1999; Meyer et al., 2015). The time resolution of the measurements is 1 Hz. Inside of ice clouds, ice water content (IWC) is calculated by subtracting the gas phase water measured by FLASH from the total water detected by FISH as described by Afchine et al. (2018). The minimum detectable IWC is 3×10^{-2} ppmv ($\sim3\times10^{-3}$ mg m^{-3}).

116

2.2. Spaceborne observation

Calibrated thermal infrared brightness temperature (BT) data at 10.8 µm wavelength, acquired every 15 min by the Spinning Enhanced Visible and Infrared Imager (SEVIRI) onboard the geostationary Meteosat Second Generation satellite (MSG) were employed to investigate the evolution of deep convection. The spatial resolution of the MSG-SEVIRI data used is 0.05° in both latitude and longitude. BT minima are generally indicative of the cloud top overshoots associated with deep convection (e.g. Kato, 2006, Lee et al., 2016).

Vertical profiles of backscatter retrieved from the Cloud-Aerosol Lidar with Orthogonal Polarization (CALIOP) on board CALIPSO (Winker et al. 2009) with a wavelength at 532 nm are used. CALIOP provides observations of particles, including high clouds, with a very high sampling resolution, 30 and 335 m in the vertical and horizontal directions, respectively.

2.3. Cloud-resolving numerical simulation

The target convective overshoots and the moistened TTL were simulated using the non-hydrostatic numerical research model, Meso-NH (Lac et al. 2018). For a fine-scale analysis, the simulation uses about 400 million grid points with horizontal grid spacing of 2.5 km. The vertical grid has 144 stretched levels (Gal-Chen and Somerville, 1975) with a spacing of 250 m in the free troposphere and the stratosphere and a finer resolution of 100 m close to the surface and between 16 and 19.5 km inside the TTL. The simulation domain covers northern India and China (Fig. 1, 5000 km × 3600 km) encompassing the track of flight #7 and the overshooting clouds over the Sichuan basin. The simulation was initialized at 00:00 UTC on 6 August 2017 and the initial and lateral boundary conditions are provided by the operational European Centre for Medium-Range Weather Forecasts (ECMWF) analyses every 6 hours. It ran for 3 days providing outputs every 1 hour.

The model employs a 1-moment bulk microphysical scheme (Pinty and Jabouille, 1998), which governs the equations of six water categories (water vapour, cloud water, rainwater, pristine ice, snow and graupel). For each particle type, the sizes follow a generalized Gamma distribution while power-law relationships allow the mass and fall speed to be linked to the diameters. Except for cloud droplets, each condensed water species has a nonzero fall speed. The turbulence parametrisation is based on a 1.5-order closure (Cuxart et al., 2000) of the turbulent kinetic energy equation and uses the Bougeault and Lacarrere (1989) mixing length. The transport scheme for momentum variables is the weighted essentially non-oscillatory (WENO) scheme of 5th order (Shu and Osher, 1988) while other variables are transported with the

piecewise parabolic method (PPM) scheme (Colella and Woodward, 1984), a scheme with excellent mass-conservation properties and low numerical diffusion (Muller, 1992).

To assess the simulation, airborne measurement data (along about 85.2°E, 25−26.5°N, blue line in Fig. 1) between 06:20 and 06:48 UTC on 8 August 2017 are compared to the simulation results averaged in a box (85−85.5°E, 25−26.5°N, marked by 'HYD' in Fig. 1) at 06:00 UTC on the same day. The CALIOP backscatter coefficients are compared to those simulated from the model outputs using the Meso-NH lidar simulator, which takes into account all the predicted scattering particles (Chaboureau et al. 2011). The SEVIRI/MSG BTs are compared to synthetic BTs computed offline using the Radiative Transfer for TIROS Operational Vertical Sounder (RTTOV) code version 11.3 (Saunders et al. 2013) from the simulation outputs (Chaboureau et al. 2008).

In this study, a 'hydration patch' is defined as a region with a water vapour amount larger than the background value at 410 K isentropic level. The background equals 5.2 ppmv which corresponds to the water vapour averaged in the box 74−84°E, 15−25°N (shown with dashed line in Fig. 1). Such a hydration patch is located within the moist layer (ML) of 18−19 km altitude (see Figure 2), corresponding to an enhanced value of water vapour observed during the last descending of flight #7 (see section 3.1). Below the hydration patch, the ice layer (IL) is located between 17 and 18 km, where an increase of ice content is observed during the same period. The hydration patch is chased visually back in time every hour from 06:00 UTC on 8 August to 13:00 UTC on 6 August 2017 (for more details, see Figure S1 in the Supplement), considering the prevailing wind direction and speed at 410 K isentropic altitude. At 14:00 UTC, a large amount of water vapour ($\geq$ 6.6 ppmv), that is injected by the convective overshoot in the Sichuan basin, starts to appear at this altitude, generating a hydration patch. With the dominant north-easterlies (15−20 m s^{-1}), it travels to the south of Kathmandu. The area of the hydration patch is about 6,000 km^2, but it is reduced to one fourth to about 1,500 km^2 during the initial overshooting phase in the convective region. This domain is used to calculate the average values of water vapour, ice content, temperature, and relative humidity displayed in Figures 9, 10, and 11.

To understand the processes along the pathway of the hydration patch, four analysis times are selected: 1) a few hours before the overshoot development at 13:00 UTC on 6 August, 2) the overshoot development time at 21:00 UTC on the same day, 3) a few hours after the overshoots at 12:00 UTC on 7 August, and 4) the aircraft measurement time at 06:00 UTC on 8 August 2017. There exist several tropopause definitions,

considering temperature lapse rate, potential vorticity, and static stability (WMO, 1957; Maddox and Mullendore, 2018). In this study, the overshoots are defined as convective cloud tops that reach the lowermost stratosphere above 380 K level. This simple definition is sufficient enough to study the impact of convective hydration on the TTL as it quickly returns to its undisturbed state (Dauhut et al., 2018). A tracer of tropospheric air is also calculated on line during the Meso-NH run. At the simulation initiation, the tropospheric and stratospheric air masses are divided by a boundary at 380 K level, and the tracer values are set to 1 and 0 below and above, respectively. In other words, pure concentration of tropospheric (stratospheric) air has tracer value equal to 100 (0) %.

3. Convective hydration in the TTL

3.1. Moistened layers in the TTL

FISH and FLASH instruments on board flight #7 measure moisture and ice content in the TTL to the south of Kathmandu along the track of ~85.2°E, 25−26.5°N (blue line in Fig. 1) from 06:20 to 06:48 UTC on 8 August 2017. ML and IL were observed. ML is evident at altitudes of 18−19 km by the water vapour content of 4.8−5.7 ppmv (solid line in Fig. 2a), and IL is apparent at altitudes of 17−18 km with the ice content of up to 1.9 eq. ppmv (solid line in Fig. 2b) and water vapour of 3.3−5.0 ppmv (solid line in Fig. 2a). The temperature minimum, which defines the cold point tropopause (CPT, red line in Fig. 2c), equals −83.5°C at 17.8 km in between ML and IL (black line in Fig. 2c). In ML, the potential temperature ranges between 394 and 428 K, while in IL it ranges between 372 and 393 K (blue line in Fig. 2c). Figure 2d shows that RH_{ice} increases beyond 70 % in ML and IL, and that IL is partly super-saturated with RH_{ice} up to 118 %. In both ML and IL, strong easterly wind prevails (black line in Fig. 2e) with wind speed exceeding 20 m s^{-1} (blue line in Fig. 2e), while easterlies stronger than 30 m s^{-1} are seen at 17 and 18.5 km altitudes.

Figure 2 also evidences that Meso-NH succeeds in reproducing most of the measurements in the TTL. It reproduces the enhanced amount of water vapour in both ML and IL. In ML, the simulated water vapour in the range between 4.9−6.0 ppmv with an average value (black cross marks in Fig. 2a) of 5.5 ppmv reproduces the measured 4.2−5.6 ppmv well. In IL, the appearance of ice (black cross marks in Fig. 2b) is simulated, but with a maximum value of 0.65 eq. ppmv, a factor of 3 less compared to the measured concentrations. The simulation captures well the CPT at 17.8 km altitude and −83.3°C (cross marks in Fig.

203   2c), RH_{ice} values of 70−100 % between 16.5−18.5-km altitudes (cross marks in Fig. 2d), and the strong

204   easterly wind (black and blue cross marks in Fig. 2e). Despite small vertical variations in water vapour and

205   temperature that are missing around the CPT, the simulation is good enough to being used to investigate the

206   source and the pathways of water in ML and IL.

207   A few hours before the Geophysica measurements and upstream, some clouds were observed in the

208   TTL by CALIOP around 20:00 UTC on 7 August 2017. Figure 3a shows a V-shaped region of strong

209   backscatter values of 0.001−0.008 km^{-1} sr^{-1} from 15 to 18.5 km altitudes over India along the track of

210   25.5−31.5°N (yellow line in Fig. 1). The V-shaped strong backscatter region is successfully reproduced by

211   Meso-NH (Fig. 3b) at 15−18.5-km altitudes between 26.5 and 31°N but with backscatter values lower than

212   measured. The simulated V-shaped region is characterized by low ice content ($\geq$ 0.1 eq. ppmv, Fig. 3c) while

213   an above-background amount of water vapour of 5−7 ppmv is layered at altitudes higher than 18 km, (Fig.

214   3d), where ML is located. The V-shaped strong backscatter region is possibly induced by waves propagating

215   at these high altitudes, e.g. gravity waves. Investigating the mechanism at its origin is however beyond the

216   scope of this article. It is worth noting that the above-background water vapour concentration and the ice

217   content are already upstream (93−95°E) about 10 hours before flight #7 (~85.2°E) and that Meso-NH is able

218   to resolve clouds in the UTLS.

219

220   *3.2. Target convective overshoots*

221   In the region where ML and IL are located, the simulated hydration patch (water vapour $\geq$ 5.2 ppmv) is in

222   evidence at the 410 K level at 06:00 UTC on 8 August 2017 (Fig. 4a). It is positioned above high-level

223   clouds, as shown with BT values lower than −47°C in both the SEVIRI/MSG imagery and the Meso-NH

224   simulation in Fig. 5a and 5b (pointed by arrows), respectively. This hydration patch has been advected from

225   the east by the strong easterlies (about 25 m s^{-1}, see Fig. 2e). At 12:00 UTC on 7 August, it is located around

226   eastern India (Fig. 4c) and is associated with low BT values ($\leq$ −55 °C) in both the MSG/SEVIRI imagery

227   (pointed by an arrow in Fig. 5c) and the Meso-NH simulation (Fig. 5d). This suggests that the hydration

228   patch is generated by the injection of water by convective overshoots. The convective overshoots start to be

229   seen from 14:00 UTC on 6 August over the Sichuan basin (Fig. 4e), and they develop in this region until

230   21:00 UTC. During the period between 14:00 and 21:00 UTC, the developing overshoots collectively inject a

231   large water vapour hourly budget of 896 t above the CPT (as the result of integrating the water vapour

232   content between two isentropic altitudes of 380 and 530 K). The signature of overshoots is evidenced over

233   the Sichuan basin at 21:00 UTC by the large amount of water vapour in excess of 18 ppmv at 410 K level

234   (Fig. 4d) and by BT values lower than −80°C (Fig. 5e and 5f). At 13:00 UTC before the overshoot

235   development, neither water vapour mixing ratio larger than 5 ppmv nor BT values lower than −60°C are

236   distinguishable over the Sichuan basin (box in Fig. 5g and 5h).

237   In summary, a good agreement is achieved between the measurements (airborne and spaceborne) and

238   the Meso-NH simulation. The analysis of the simulation shows that the water-enhanced layers in ML and IL

239   observed to the south of Kathmandu around 06:30 UTC on 8 August were generated by the injection of water

240   by the convective overshoots produced over the Sichuan basin during 14:00−21:00 UTC on 6 August.

241

242   **4. Pathway of the hydration patch and processes affecting it**

243   *4.1. Evolution of the hydration patch during its way to the south of Kathmandu*

244   The hydration patch is described along its way from the Sichuan basin to the south of Kathmandu. In the

245   following, vertical sections of water vapour, ice content and tropospheric tracer are shown across the

246   hydration patch in the west-east orientation every 2 to 6 h (Figs. 6, 7, and 8). The vertical cross-sections are

247   centred over the hydration patch, all with the same size.

248

249   *4.1.1. Injection of water into the TTL by convective overshoots*

250   The vertical cross-sections of water vapour and ice content evidence that the large amounts of water vapour

251   and ice are injected above 380 K level by the convective overshoots that occurred during 15:00−21:00 UTC

252   on 6 August. At 13:00 UTC (Fig. 6a), just before the overshoot development, a strong upward motion is seen

253   at 16−18-km altitudes, while the cloud top (black solid line) is located in IL (about 17.5 km), just below the

254   CPT. At 15:00 UTC (Fig. 6b), a large amount of water vapour (≥ 15 ppmv) is in evidence in ML above 410

255   K level while a large ice content in excess of 120 eq. ppmv is found in IL, between 380 and 410 K levels

256   (Fig. 7b). Figure 8a−b shows that during 15:00−17:00 UTC the concentration of the tropospheric tracer

257   increases in both ML and IL with values of 4 and 30 %, respectively.

258   At 17:00 UTC and even higher cloud top is apparent at ~19.5 km altitude (Fig. 6c), a large amount of

259   water vapour (≥ 18 ppmv) rises to ~20 km, around 103°E, and a large ice content (≥ 120 eq. ppmv) stays

260   below 18 km altitude (Fig. 7c). The large amount of water is directly injected by convective overshoots

261   mainly in the form of ice, as the ice-laden air within the convective overshoots mixes with the entrained

262   stratospheric air during the collapse of the overshooting top. The warm, sub-saturated stratospheric air causes

263   the ice to rapidly sublimate into water vapour at the top of the overshoot, moistening the layer. It is worth

264   noting the water injected by the convective overshoots at 15:00 UTC is still apparent in ML at 17:00 UTC

265   around 102°E with a water vapour mixing ratio above 9 ppmv (Fig. 6c). In a similar way, the convectively-

266   injected large moisture at 17:00 UTC around 103°E (Fig. 6c) is found in ML at 19:00 UTC around 102.5°E

267   with a water vapour mixing ratio larger than 15 ppmv (Fig. 6d). At 19:00 UTC (Fig. 6d), the strong

268   convective updraughts perturb the isentropic surfaces (red solid lines), descending the 410 K level largely

269   from about 18.5 to 17.5 km. At 21:00 UTC a higher cloud top is found above ML in a wide area

270   (102.3−103.3°E longitude). The injected water vapour (≥18 ppmv) is transported above 20.5 km (Fig. 6e)

271   while the concentration of 0.1−0.5 % of the tropospheric tracer is seen in the water vapour pocket. The large

272   ice content exceeding 120 eq. ppmv is distributed mostly in IL (Fig. 7e). During 15:00−21:00 UTC (Fig.

273   8b−e), a concentration of 2−20 % of the tropospheric tracer is consistently seen in ML, while higher

274   concentration of 40 % has been found in IL. During 17:00−21:00 UTC (Fig. 9c−e), the large turbulent

275   kinetic energy (TKE) of 0.2−0.9 $m^2\ s^{-2}$ is apparent in a limited area of cloud top (~103°E).

276   *4.1.2. Evolution of the hydration patch along its pathway*

277   From 23:00 UTC on 6 August to 06:00 UTC on 8 August 2017, the convective overshoots gradually

278   diminish in the region of longitude ~98−85°E and latitude ~28−25°N (see Fig. 4). At 23:00 and 00:00 UTC,

279   the anvil-shaped cloud above 16 km altitude presents a rather flat cloud top around 19 km (Fig. 7f and 7g).

280   The injected large amount of water vapour ≥ 18 ppmv is evident in ML, even at higher altitudes up to 20.5

281   km (Fig. 6f and 6g) whereas the large ice content ≥ 120 eq. ppmv is no longer apparent in IL (Fig. 7f and 7g).

282   Within the anvil cloud, still large TKE of 0.2−0.9 $m^2\ s^{-2}$ is seen (Fig. 9f, g). During 06:00−18:00 UTC on 7

283   August, the water vapour mixing ratio in ML gradually decreases from 15 to ~9 ppmv, meanwhile the air

284   mass in IL becomes dry with a water vapour mixing ratio below 4 ppmv (Fig. 6h−j). During the same period,

285   the increase of tropospheric tracer concentration and TKE are evident in both ML and IL. The air mass with

286   concentration higher than 40 % is apparent in IL while the air mass with a lower tropospheric concentration

287   around 0.02−0.3 is seen in IL (Fig. 8h−j).

288   The air mass with high tropospheric tracer concentration of 2−40 % consistently exists in ML and IL

289   from 00:00 to 06:00 UTC on 8 August 2017 (Fig. 8k−l), while the TKE of 0.2−0.9 $m^2\ s^{-2}$ exists in wide area

between the altitudes of 16 and 18 km (Fig. 9k−l). During this period, the hydration patch is further narrowed and widened in ML (Fig. 6k−l), and the air mass becomes drier in IL (≤ 3 ppmv). Note that the even low numerical diffusion of the PPM scheme also contributes to the dispersion of the hydration patch. At 00:00 UTC (Fig. 7k), new convection tops are apparent in altitudes of 16−17 km, and an increase of ice content above 3 eq. ppmv is seen in IL. Then a decrease of ice content down to 0.1−1 eq. ppmv distributes in IL at 06:00 UTC where large ice content around 1−1.9 eq. ppmv was measured (see Fig. 2b).

4.2. Processes affecting the hydration patch

The processes that affect the moist and ice layers are further described. To this objective, average quantities are calculated in ML and IL. The hourly evolution of water vapour, ice content, temperature, and RH_{ice} shows the lifetime of the injected water in ML and IL along the pathway of the hydration patch (Fig. 10). The profiles of tropospheric tracer, temperature, RH_{ice}, water vapour, ice content and wind speed give a vertical view in the column across the tropical tropopause layer (Fig. 11). A scatter plot using tropospheric tracer and water vapour highlights the mixing processes occurring in the hydration patch (Fig. 12).

4.2.1. Mixing of the overshoots with the stratospheric air

The hourly evolution of the average water vapour and the ice content along the pathway of the hydrated layer demonstrates the hydration in the TTL by the convective overshoots (Fig. 10). During the development of the convective overshoots between 14:00 and 21:00 UTC on 6 August 2017, the average water vapour mixing ratio increases to 5.7 ppmv in IL (yellow solid line, Fig. 10a), while a large mixing ratio of 6.5 ppmv is seen in ML (blue solid line in Fig. 10a). The ice content reaches more than 200 eq. ppmv in both layers and more than 300 eq. ppmv in IL (Fig. 10b). Until 17:00 UTC, the temperature increases in both layers (solid lines in Fig. 10c), indicating the mixing with the warmer stratospheric air. Because of this entrained stratospheric air, RH_{ice} decreases largely below 60 % in ML (blue line with symbols in Fig. 10c), and down to 90 % in IL (yellow line with symbols). Due to the mixing with entrained warmer stratospheric air, the enriched water vapour layer then remains at this higher isentropic level after the overshoot collapses. The conditions and timescale of the detailed process trapping the enriched water vapour in the TTL was demonstrated by Dauhut et al. (2018). Thanks to a fine temporal resolution of 1 min, they revealed that this process occurs on short time scales within 20 min. The active mixing of the convective overshoots with the stratospheric air between

319   14:00 and 21:00 UTC is also evidenced by the evolution of vertical profiles of tropospheric tracer (Fig. 11a).

320   The tropospheric tracer concentration increases from 0 to 5 % in ML (yellow to green lines in Fig. 11a),

321   while the stratospheric air concentration (1 minus tracer) increases of 5 % in IL. The temperature increases in

322   both ML and IL (yellow to green lines in Fig. 11b) where the relative humidity decreases (yellow to green

323   lines in Fig. 11c).

324   The scatter plot of the tropospheric tracer and water vapour mixing ratio (Fig. 12) evidences the large

325   mixing of tropospheric and stratospheric air masses in the TTL (14−22 km altitudes). A large evolution of the

326   tropospheric tracer−water vapour diagram is found from 13:00 to 21:00 UTC on 6 August (Fig. 12a and

327   12b). At 13:00 UTC before the development of the convective overshoots, the air mass with potential

328   temperature (θ) of 410−420 K (yellow dots), corresponding to ML, is relatively dry with a water vapour

329   mixing ratio of 5−7.2 ppmv (Fig. 12a) and very small compounds of tropospheric air (tracer ≤ 0.1 %). The

330   air mass with θ of 380−390 K (black dots), corresponding to IL, has a low water vapour mixing ratio of

331   3−7.5 ppmv. At 21:00 UTC (Fig. 12b), the air mass with θ between 410 and 420 K becomes very humid

332   (5.5−13.6 ppmv of water vapour) and the concentration of tropospheric tracer increases to 0.2−8 %.

333   Moreover the air mass with very-high θ of 450−460 K (purple dots) is moistened largely as shown by a water

334   vapour mixing ratio above 15 ppmv. So does the air mass with θ between 390 and 410 K, which is both

335   moistened and enriched by the tropospheric tracer with a concentration of 5−60 % (red to orange dots, Fig.

336   12b). The convective overshoots also impact the air mass below the CPT by widening the range of the water

337   vapour mixing ratio with θ between 370 and 380 K (grey dots in Fig. 12a and b) from 3.2−13.9 ppmv at

338   13:00 UTC (Fig. 12a) to 0−18.8 ppmv at 21:00 UTC (Fig 12b).

339   From 17:00 UTC on 6 August to 02:00 UTC on 7 August, Fig. 9c shows that the temperature

340   decreases gradually (solid lines), while the relative humidity increases (lines with symbols). In ML and IL, a

341   great part of ice contents, especially snow and graupel fall quickly (dashed line in Fig. 10b), and the rest

342   sublimates. Meanwhile ice sediment out, still there is a low concentration of cloud ice in both ML and IL,

343   and the water vapour concentration slightly decreases (blue solid line in Fig. 10a). The continued presence of

344   cloud ice in ML suggests that the ice may have formed in-situ in response to wave-driven temperature

345   oscillations that locally drive the RH to ice saturation. The ice microphysics might play a pivotal role in

346   controlling the eventual moisture content since ice nucleation and the subsequent ice-growth process to

347   deplete slowly the ML. In ML, the relative humidity increases (in range of 65−80 %) mainly due to the

348   temperature decrease (in range of −78 and −82°C) (solid lines, Fig. 10c). During this period, the easterly

349   wind is nearly constant with the relatively-weak speed of ~15 m s^{-1} in ML and ~16.5 m s^{-1} in IL (yellow to

350   green lines, Fig. 11f). After 7 August, in ML, the relative humidity less than 80 % indicates strong sub-

351   saturation where a very small amount (0.1−0.3 eq. ppmv) of cloud ice still resides. This is probably induced

352   by the domain-averaged analysis.

353

354   *4.2.2. Processes occurring in the hydration patch during the advection*

355   After the development of the convective overshoots, the hydration patch travels westward across India and

356   north Bangladesh from 21:00 UTC on 6 August to 06:00 UTC on 8 August (Fig. 4). During its travel, the air

357   mass in ML and IL has less and less amount of water vapour and ice content (Fig. 10a−b).

358   Between 21:00 UTC on 6 August and 12:00 UTC on 7 August, the concentration of tropospheric tracer

359   increases at high altitudes with θ between 410 and 420 K up to 18 % (yellow dots, Fig. 12b−c). At the same

360   time, the water vapour decreases by a factor of two, in the range of 5−9.6 ppmv. This can be also seen in the

361   vertical profiles for which the concentration of tropospheric tracer increases at 12:00 UTC on 7 August in

362   both ML and IL (green to blue lines, Fig. 11a) and the water vapour decreases (green to blue lines, Fig. 11d).

363   The two layers become colder by ~3°C (green to blue lines in Fig. 11b), and dehydrated compared to the

364   initial state of 13:00 UTC on 6 August (yellow line in Fig. 11d, e). It includes much reduced amount of ice

365   content (green to blue solid lines in Fig. 11e), but still there exist ice content ≥ 1 eq. ppmv and cloud ice ≥

366   0.5 eq. ppmv at 12:00 UTC on 7 August (blue dashed line, Fig. 11e). In IL (Fig. 10c), RH_{ice} oscillates mostly

367   driven by temperature variation. Over time, the air mass in ML and IL gets colder and less humid by the

368   lowered cloud top below 17 km altitude. In both ML and IL, the easterly winds weaken below 15 m s^{-1}.

369   Moreover, the turbulent kinetic energy (TKE) increases from 0.1−0.3 m^2 s^{-2} at 21:00 UTC to 0.2−0.9 m^2 s^{-2}

370   at 12:00 UTC in ML and IL (Fig. 9e, i). These results suggest that the water vapour concentration in ML and

371   IL decreases due to the turbulent diffusion in both the vertical and the horizontal direction consistent with the

372   increase of tropospheric tracer. Also, the vapour-scavenging effect by ice nucleation and particle growth

373   within IL contributes to reduce the water vapour deriving the dehydration. The rapid decrease of ice content

374   in IL due to both sublimation and sedimentation (Fig. 7f−i) results in the lowering of the cloud top from 17

375   to below 16 km at 97−101°E at 06:00 UTC (Fig. 7h), and finally to 15 km around 95.5°E at 12:00 UTC (Fig.

376   7i).

Further increased tropospheric tracer concentration is distinguished from 12:00 UTC on 7 August to 06:00 UTC on 8 August 2017 in ML and IL (blue to red lines, Fig. 11a). Moreover the tropospheric tracer concentration reaches to about 30 and 70 % in ML and IL, respectively while the water vapour decreases (Fig. 11a and 11d). During this time, the cloud top height of convective cloud descends below 14 km (Fig. 6i−l), where RH_{ice} dramatically decreases (Figs. 2d, 11c). The entrained cold tropospheric air (and/or colder background air) and the hydrostatic adjustment decrease the temperature in ML and IL (Fig.11b). It is worth noting the shape of the temperature profile that becomes straight upward in the altitudes of 17−18.5 km during the overshoot activity (green line, Fig. 11b). Also it is worth noting the decrease of ice content less than 0.3 eq. ppmv (blue to red line, Fig. 11e), and the large-decrease of relative humidity in altitudes below 17.5 km.

The increased tropospheric tracer concentration in ML and IL is as well seen by the tracer−vapour diagram of Fig. 12c−d. The concentration of tropospheric tracer increases at high altitudes with θ between 410 and 420 K (yellow dots) up to 20 % at 06:00 UTC on 8 August 2017, meanwhile the tropospheric air concentration increases up to 50 % at the altitudes with θ between 390 and 400 K (red dots in Fig. 12d). During the period (12:00 UTC on 7 August to 06:00 UTC on 8 August), the water vapour decreases in all altitudes with θ above 380 K (Fig. 12c−d). It decreases from 9.6 to below 6.2 ppmv in ML (θ between 410−430 K, yellow and green dots) while dropping below 5 ppmv in IL (θ between 380−400 K, red and black dots). The reduced ice content in ML and IL might be induced by sublimation due to the mixing with the dry tropospheric air (RH_{ice} ~50−70 %) of below 16 km level (red line in Fig. 11c and cross marks in Fig. 2d). The air mixing of tropospheric and stratospheric air masses might be induced by the vertical wind shear with the maxima wind speeds in excess of 30 m s^{-1} at ~17 and 18.5 km altitudes (see Fig. 2e, average value in range of 18 and 25 m s^{-1} of red line in Fig. 11f). With the strengthened easterlies, the air mass in IL is well mixed rather than conserved in this layer. Also, this wind shear layer with a large gradient of wind speed (25–35 m s^{-1}) locates below and above the CPT (Fig. 2c, 2e), thus it results in the strait upward temperature profile with the constant value about −80°C at 06:00 UTC on 8 August as seen in Fig. 10b (red line). The air mass in ML and IL has large TKE values of 0.5 m^2 s^{-2} (Fig. 9l).

5. Conclusions

The source and pathway of the hydration patch in the TTL (Tropical Tropopause Layer) that was measured

406 during flight #7 of the StratoClim 2017 field campaign during the Asian summer monsoon, and its

407 connection to overshooting convection are investigated. During the Geophysica flight #7 around 06:30 UTC

408 on 8 August 2017, two remarkable layers were observed to the south of Kathmandu above and below the

409 CPT located at 17.8 km, a moist layer (ML) with large water vapour content of 4.2−5.6 ppmv in altitudes of

410 18−19 km in the lower stratosphere, and an ice layer (IL) with large ice content up to 1.9 eq. ppmv at

411 altitudes of 17−18 km in the upper troposphere. The Meso-NH numerical simulation run with a 2.5 km

412 horizontal grid spacing succeeds in reproducing ML and IL. Through analysis using airborne and spaceborne

413 measurements and the numerical simulation, we show that the measured hydration patch in ML found in the

414 south of Kathmandu (~85°E) was produced by the convective overshoots that occurred over the Sichuan

415 basin (~103°E) between 14:00 and 21:00 UTC on 6 August 2017. The key hydration processes are

416 summarized schematically in Fig. 13.

417   The convective overshoots develop up to 19.5 km altitude in the Sichuan basin, and transport large

418 amount of water vapour of 6.5 ppmv to ML and ice content in excess of 300 eq. ppmv to IL. Between 15:00

419 and 21:00 UTC, the overshooting clouds collectively hydrate the lower stratosphere resulting in the total

420 amount of water vapour of 6088 t. It is also worth noting the large concentration of water vapour of over 18

421 ppmv up to 20 km level which is above the convective cloud top of 19.5 km (a yellow ellipsoid in Fig. 13a).

422 This feature is similarly seen during the development of the Hector the Convector in the Tiwi Islands

423 (Dauhut et al., 2018), however, the magnitude is ~10 ppmv higher in the present event. The concentration of

424 the tropospheric tracer reaches to 8 and ~60 % in ML and IL, respectively, indicating the strong mixing of

425 the convective updraughts with the stratospheric air (black arrows in Fig. 13a). The strong convective

426 updraughts perturb the isentropic surfaces (red line in Fig. 13a), descending the 410 K level from 18.5 to

427 17.5 km. During these convective events, the mixing of the tropospheric and stratospheric air masses

428 increases the temperature in ML and IL. Moreover, the moderate -not intense- easterly wind (~15 m s^{-1})

429 prevails constantly in these levels, and it does not interrupt the convection developing vigorously in altitude

430 (19.5 km ASL) and reaching the lower stratosphere.

431   The injected water by the convective overshoots generates the hydration patch, i.e. large water vapour

432 in ML (ellipse in Fig. 13b). During its westward travel, its altitude is kept constant by the moderate easterlies

433 of about 15 m s^{-1} in ML and IL. The tropospheric tracer concentration is continuously increased in these

434 layers, where the above-background amount of water vapour is still remained and where the ice content

gradually sediments out and forms again along the pathway. It is highlighted that the large transported amount of water vapour ($\geq$18 ppmv) still remains at high altitudes of up to 20.5 km even when the anvil cloud top descends to 18.5 km. Later on, the cloud top is still seen around 16−17 km level, keeping the large RH_{ice} (about 95 %) in these altitudes. A part of the water vapour has been lost due to ice formation and sedimentation and the turbulent diffusion in both vertical and the horizontal direction (black arrows in Fig. 13b). The ice microphysics (e.g. nucleation, growth, and sedimentation of ice particles) might play a pivotal role in controlling the eventual moisture content since ice nucleation and the subsequent growth process would slowly deplete the water vapour. This falling of ice and a reduced updraught are evident by the lowered cloud top height partly from 17 to ~15 km (Fig. 13c).

Then the hydration patch continues to travel to the south of Kathmandu, with even higher tropospheric tracer concentration of ~30 and 70 % in ML and IL, respectively (darkened blue shades in Fig. 13c). During the same period, the top of convective clouds further descends below 14 km, thus the layer below IL, i.e. 15−17 km, becomes dry with RH_{ice} below 70 %. Due to mixing with the dry tropospheric air, the remaining water vapour in ML gradually diffused in horizontal and vertical direction (ellipse). It is also true that the ice content in IL is locally influenced by new convection with cloud top in altitudes 16−17 km about 6 h before flight #7. The continuous air mixing might be induced by the vertical wind shear in altitudes 15−19 km where the wind speed varies from ~18 to 25 m s^{-1} (red bold arrows in Fig. 13c). The vertical mixing due to wind shear modifies the temperature profile to the straight-upward in 17−18 km rather than bending. Also, vertical motions caused by gravity waves breaking might play an important role in the transport of tropospheric air into the TTL. In addition, after the strong updraughts of overshooting convection, the remaining horizontal divergence in the lower stratosphere might let the tropospheric air continues to ascend.

Many of previous Lagrangian studies (Tzella and Legras, 2011; Tissier and Legras, 2016) demonstrated the link between the moistened TTL and remote overshoots using large-scale numerical simulations. Thanks to the combination of aircraft measurement and a 3-day convection-permitting simulation, this study shed light on the processes along the pathway of a hydration patch from overshooting clouds for 1.5 days, showing the 3-D evolution of water vapour and ice content.

This study focuses on the hydration patch that was measured during the last descending of flight #7 and the corresponding convective overshoots over the Sichuan basin. Here, the average water vapour amount in the lower stratosphere is 6.5 ppmv during the convective event while a water vapour of 6 ppmv is found

464 above West Africa during the monsoon season by Khaykin et al. (2009). By comparison, convection

465 developing during the Asian monsoon over the Sichuan basin had a similar impact on the stratospheric water

466 budget as above West Africa. From the hourly budget of 869 t, we can also confirm that the local impact of

467 overshoots developed during the Asian summer monsoon is stronger than the one over tropical Africa

468 (300−500 t according to Liu et al., 2010) and is weaker than Hector the Convector over the Tiwi Islands

469 (2776 t according to Dauhut et al., 2015). Because of a large variety in the lifetime and horizontal scale of

470 overshoots, an accumulation of more event-scale analyses is important. In addition, note that the amount of

471 injected moisture is sensitive to the grid spacing of simulation (up to a factor of 2 with horizontal grid

472 spacing varying from 1600 to 100 m; Dauhut et al., 2015) and the convection duration of target system. The

473 simple set up of tropospheric tracer of this study, i.e. tropospheric air below the 380 K isentropic altitude,

474 allows the mixture of tropospheric and stratospheric air parcels in the TTL by vigorous convective

475 overshoots to be understood. To estimate the detailed origin i.e. defining the lower, middle, and upper

476 troposphere, of air parcel, further analyses using passive tracers (e.g. Mullendore et al., 2005; Hassim and

477 Lane, 2010; Homeyer, 2015; Dauhut et al., 2016) will be required. Also, additional numerical simulation

478 with a 2-moment microphysical scheme that considers mass and number concentration of hydrometeors and

479 aerosol together with options in the turbulent scheme (e.g., 1D against 3D formulation, Machado and

480 Chaboureau, 2015) will be worthwhile to study the impact on the results. To understand how much water

481 vapour and ice are generally injected into the TTL through convective overshoots during the Asian summer

482 monsoon is currently investigated in a follow-up study. Further, it would be interesting to investigate the

483 transport of chemical constituents, e.g. methane, nitrogen oxides, and carbon monoxide, via convective

484 overshoots during this season.

485

486 **Data availability**

487 After the StratoClim embargo period, the aircraft data will be freely available. Meso-NH output data are

488 available from JPC upon request.

489

490 **Author contribution**

491 KOL, TD and JPC designed the numerical simulation, and JPC performed the simulation. KOL, TD and JPC

492 designed the manuscript and analyses. SK provided the FLASH instrument data, and MK and CR provided

493   the FISH instrument data. KOL prepared the manuscript with contributions from all co-authors.

494

Acknowledgement

496   This study is funded by the StratoClim project by the European Union Seventh Framework Programme

497   under grant agreement no 603557 and the Idex TEASAO project. Computer resources were allocated by

498   GENCI through project 90569.

499

References

501   Afchine, A., Rolf, C., Costa, A., Spelten, N., Riese, M., Buchholz, B., Ebert, V., Heller, R., Kaufmann, S.,

502   Minikin, A., Voigt, C., Zöger, M., Smith, J., Lawson, P., Lykov, A., Khaykin, S., and Krämer, M.: Ice

503   particle sampling from aircraft – influence of the probing position on the ice water content, Atmos.

504   Meas. Tech., 11, 4015-4031, https://doi.org/10.5194/amt-11-4015-2018, 2018.

505   Bougeault, P. and Lacarrère, P.: Parameterization of orography-induced turbulence in a meso-beta-scale

506   model. Mon. Weather Rev. 117(8): 1872−1890, https://doi.org/10.1175%2F1520-

507   0493%281989%29117%3C1872%3APOOITI%3E2.0.CO%3B2, 1989.

508   Chaboureau, J.-P., Cammas, J.-P.,Duron, J., Mascart, P. J., Sitnikov, N. M., and Voessing, H. J.: A numerical

509   study of tropical cross-tropopause transport by convective overshoots, Atmos. Chem. Phys., 7, 1731–

510   1740, https://doi.org/10.5194/acp-7-1731-2007, 2007.

511   Chaboureau, J.-P., and Coauthors: A midlatitude precipitating cloud database validated with satellite

512   observations. J. Appl. Meteor. Climatol., 47, 1337–1353, https://doi.org/10.1175/2007JAMC1731.1,

513   2008.

514   Chaboureau, J.-P., and Coauthors: Long-range transport of Saharan dust and its radiative impact on

515   precipitation forecast: A case study during the Convective and Orographically-induced Precipitation

516   Study (COPS). Quart. J. Roy. Meteor. Soc., 137, 236–251, https://doi.org/10.1002/qj.719, 2011.

517   Colella, P. and Woodward, P. R.: The piecewise parabolic method (PPM) for gas dynamical simulations. J.

518   Comput. Phys. 54: 174−201, https://doi.org/10.1016/0021-9991(84)90143-8, 1984.

519   Cuxart, J., Bougeault, P., and Redelsperger, J. L.: A turbulence scheme allowing for mesoscale and large-

520   eddy simulations. Q. J. R. Meteorol. Soc. 126(562): 1−30, https://doi.org/10.1002/qj.49712656202,

521   2000.

Dauhut, T., Chaboureau, J. P., Escobar, J., and Mascart, P.: Large-eddy simulations of hector the convector making the stratosphere wetter. Atmos. Sci. Let. 16, 135−140, https://doi.org/10.1002/asl2.534. 2015.

Dauhut, T., Chaboureau, J. P., Escobar, J., and Mascart, P.: Giga-LES of hector the convector and its two tallest updrafts up to the stratosphere. J. Atmos. Sci., 73, 5041−5060, https://doi.org/10.1175/JAS-D-16-0083.1, 2016.

Dauhut, T., Chaboureau, J. P., Haynes, P. H., and Lane, T. P: The mechanisms leading to a stratospheric hydration by overshooting convection. J. Atmos. Sci., 75, 4383-4398, https://doi.org/10.1175/JAS-D-18-0176.1, 2018

Dessler, A. E. and Sherwood, S. C.: Effect of convection on the summertime extratropical lower stratosphere, J. Geophys. Res., 109, D23301, https://doi.org/10.1029/2004JD005209, 2004.

Fueglistaler, S., Dessler, A. E., Dunkerton, T. J., Folkins, I., Fu, Q., and Mote, P. W.: Tropical tropopause layer, Rev. Geophys., 47, RG1004, https://doi.org/10.1029/2008RG000267, 2009.

Funatsu, B. M., Rysman, J. F., Claud, C., and Chaboureau, J. P.: Deep convective clouds distribution over the Mediterranean region from AMSU-B/MHS observations, Atmos. Res., 207, 122-135, https://doi.org/10.1016/j.atmosres.2018.03.003, 2018.

Gal-Chen, T. and Somerville, R. C. J.: On the use of a coordinate transformation for the solution of the Navier-Stokes equations. J. Comput. Phys. 17: 209−228, https://doi.org/10.1016/0021-9991(75)90037-6, 1975.

Homeyer, C. R., Pan, L. L., Dorsi, S. W., Avallone, L. M., Weinheimer, A. J., O'Brien, A. S., DiGangi, J. P., Zondlo, M. A., Ryerson, T. B., Diskin, G. S., and Campos, T. L.: Convective transport of water vapor into the lower stratosphere observed during double-tropopause events. J. Geophys. Res. Atmos., 119, 10941−10958, https://doi.org/10.1002/2014JD021485, 2014.

Homeyer, C. R.: Numerical simulations of extratropical tropopause penetrating convection, J. Geophys. Res. Atmos., 120, 7174−7188. https://doi.org/10.1002/2015JD023356, 2015.

Homeyer, C. R., McAuliffe, J. D., and Bedka, K. M.: On the development of above-anvil cirrus plumes in Extratropical convection. J. Atmos. Sci., 74, 1617−1633, https://doi.org/10.1175/JAS-D-16-0269.1, 2017

Hassim, M. E. E. and Lane, T. P.: A model study on the influence of overshooting convection on TTL water vapour, Atmos. Chem. Phys., 10, 9833−9849, https://doi.org/10.5149/acp-10-9833-2010, 2010.

Highwood, E. J., and Hoskins, B. J.: The tropical tropopause, Q. J. R. Meteorol. Soc., 124, 1579−1604, https://doi.org/10.1002/qj.49712454911, 1998.

Hoskins, B. J. and Rodwell, M. J.: A model of the Asian summer monsoon, I, The global scale, J. Atmos. Sci, 52, 1329−1340, https://doi.org/10.1175/1520-0469%281995%29052%3C1329%3AAMOTAS%3E2.0.CO%3B2, 1995.

Jensen, E., Ackerman, A. S. and Smith, J. A.: Can overshooting convection dehydrate the tropical tropopause layer? J. Geophys. Res., 112, D11209, https://doi.org/10.1029/2006JD007943, 2007.

Kato T.: Structure of the band-shaped precipitation system inducing the heavy rainfall observed over northern Kyushu, Japan on 29 June 1999. J. Meteor. Soc. Japan. 84,129−153, https://doi.org/10.2151/jmsj.84.129, 2006.

Khaykin, S. M., Pommereau, J.-P., Riviere, E. D., Held, G., Ploeger, F., Gysels, M., Amarouches, N., Vernier, J.-P., Wienhold, F. G., and Ionov, D.: Evidence of horizontal and vertical transport of water in the southern hemisphere tropical tropopause layer (TTL) from high-resolution balloon observation, Atmos. Chem. Phys., 16, 12273−12286, https://doi.org/10.5194/acp-16-12273-2016, 2016.

Khaykin, S., Pommereau, J.-P., Korshunov, L., Yushkov, V., Nielsen, J., Larsen, N., Christense, T., Garnier, A., Lukyanov, A., and Williams, E.: Hydration of the lower stratosphere by ice crystal geysers over land convective systems, 9, 2275−2287, https://doi.org/10.5194/acp-9-2275-2009, 2009.

Khaykin, S. M., Engel, I., Vömel, H., Formanyuk, I. M., Kivi, R., Korshunov, L. I., Krämer, M., Lykov, A. D., Meier, S., Naebert, T., Pitts, M. C., Santee, M. L., Spelten, N., Wienhold, F. G., Yushkov, V. A., and Peter, T.: Arctic stratospheric dehydration – Part 1: Unprecedented observation of vertical redistribution of water, Atmos. Chem. Phys., 13, 11503–11517, https://doi.org/10.5194/acp-13-11503-2013, 2013.

Lac, C., Chaboureau, J. P., Masson, V., Pinty, J. P., Tulet, P., Escobar, J., Leriche, M., Barthe, C., Aouizerats, B., Augros, C., Aumond, P., Auguste, F., Bechtold, P., Berthet, S., Bieilli, S., Bosseur, F., Caumont, O., Cohard, J. M., Colin, J., Couvreux, F., Cuxart, J., Delautier, J., Dauhut, T., Ducrocq, V., Filippi, J.B., Gazen, D., Geoffroy, O., Gheusi, F., Honnert, R., Lafore, J. P., Lebeaupin, Brossier C., Libois, Q., Lunet, T., Mari, C., Maric, T., Mascart, P., Mogé, M., Molinié, G., Nuissier, O., Pantillon, F., Peyrillé, P., Pergaud, J., Perraud, E., Pianezze, J., Redelsperger, J. L., Ricard, D., Richard, E., Riette, S., Rodier, Q., Schoetter, R., Seyfried, L., Stein, J., Suhre, K., Taufour, M., Thouron, O., Turner, S., Verrelle, S.,

580   Vié, B., Visentin, F., Vionnet, V., and Wautelet, P.: Overview of the Meso-NH model version 5.4 and

581   its applications. Geosci. Model Dev., 11, 1929-1969, https://doi.org/10.5194/gmd-11-1929-2018, 2018.

582 Lee, K. O., Flamant, C., Ducrocq, V., Duffourg, F., Fourrié, N., and Davolio, S. : Convective initiation and

583   maintenance processes of two back-building mesoscale convective systems leading tow heavy

584   precipitation events in South Italy during HyMeX IOP 13. Q. J. R. Meteorol. Soc., 142, 2623−2635,

585   https://doi.org/10.1002/qj.2851, 2016.

586 Liu, C., and Zipser, E. J.: Global distribution of convection penetrating the tropical tropopause, J. Geophys.

587   Res., 110, D23104, https://doi.org/10.1029/2005JD006063, 2005.

588 Liu, X. M., Rivière, E. D., Marécal, V., Durry, G., Hamdouni, A., Arteta, J., and Khaykin, S.: Stratospheric

589   water vapour budget and convection overshooting the tropopause: modelling study from SCOUT-

590   AMMA. Atmos. Chem. Phys., 10, 8267–8286, www.atmos-chem-phys.net/10/8267/2010, 2010.

591 Machado, L. A., and Chaboureau, J. P.: Effect of Turbulence Parameterization on Assessment of Cloud

592   Organization. Mon. Wea. Rev., 143, 3246–3262, https://doi.org/10.1175/MWR-D-14-00393.1, 2015.

593 Maddox, E. M. and Mullendore, G. L.: Determination of best tropopause definition for convective

594   transportation studies. J. Atmos. Sci., 75, 3433–3446, https://doi.org/10.1175/JAS-D-18-0032.1, 2018.

595 Mason, R. and Anderson, C.: The development and decay of the 100-MB. Summertime anticyclone over

596   southern Asia. Mon. Wea. Rev., 1, 3−12, https://doi.org/10.1175/1520-

597   0493%281963%29091%3C0003%3ATDADOT%3E2.3.CO%3B2, 1963.

598 Meyer, J., Rolf, C., Schiller, C., Rohs, S., Spelten, N., Afchine, A., Zöger, M., Sitnikov, N., Thornberry, T. D.,

599   Rollins, A. W., Bozóki, Z., Tátrai, D., Ebert, V., Kühnreich, B., Mackrodt, P., Möhler, O., Saathoff, H.,

600   Rosenlof, K. H., and Krämer, M.: Two decades of water vapor measurements with the FISH

601   fluorescence hygrometer: a review, Atmos. Chem. Phys., 15, 8521–8538, https://doi.org/10.5194/acp-

602   15-8521-2015, 2015.

603 Mullendore, G. L., Durran, D. R., and Holton, J. R.: Cross-Tropopause tracer transport in midlatitude

604   convection, J. Geophys. Res., 110, D06113, https://doi.org/10.1029/2004JD005059, 2005.

605 Müller, R.: The performance of classical versus modern finite-volume advection schemes for atmospheric

606   modelling in a one-dimensional test-bed, Mon. Wea. Rev., 120, 1407–1415,

607   https://doi.org/10.1175/1520-0493(1992)120%3C1407:TPOCVM%3E2.0.CO;2, 1992.

608 Park, M., Randel, W. J., Kinnison, E. J., Garcia, R. R., and Choi, W.: Seasonal variation of methane, water

vapor and nitrogen oxides near the tropopause: Satellite observations and model simulation, J. Geophys. Res., 109, D03302, https://doi.org/10.1029/2003JD003706, 2004.

Pinty, J. P. and Jabouille, P.: A mixed-phased cloud parametrization for use in a mesoscale non-hydrostatic model: Simulations of a squall line and of orographic precipitation. In: Proc. Of the Conference on Cloud Physics. Amer. Meteorol. Soc, Boston: Everett, WA, USA, 17−21 Aug. 1998. Pp. 217−220, 1998.

Randel, W. J. and Park, M.: Deep convective influence on the Asian summer monsoon anticyclone and associated tracer variability observed with Atmospheric Infrared Sounder (AIRS), J. Geophys, Res., 111, D12314, https://doi.org/10.1029/2005JD006490, 2006.

Randel, W. J., Wu, F., Gettelman, A., Russell, J. M., Zawodny, J. M., and Oltmans, S. J.: Seasonal variation of water vapour in the lower stratosphere observed in Halogen Occultation Experiment data, J. Geophys. Res., 106(D13), 14313−14325, https://doi.org/10.1029/2001JD900048, 2001.

Rysman, J. F., Claud, C., Chaboureau, J. P., Delanoë, J., and Funatsu, B. M.: Severe convection in the Mediterranean from microwave observations and a convection-permitting model, Quart. J. Roy. Meteor. Soc., 142, 43-55, https://doi.org/10.1002/qj.2611, 2016.

Rolf, C., Vogel, B., Hoor, P., Afchine, A., Günther, G., Krämer, M., Müller, R., Müller, S., Spelten, N., and Riese, M.: Water vapor increase in the lower stratosphere of the northern hemisphere due to the Asian monsoon anticyclone observed during the TACTS/ESMVal campaigns, Atmos. Chem. Phys., 18, 2973−2983, http://doi.org/10.5194/acp-18-2973-2018, 2018.

Saunders, R., Hocking, J., Rundle, D., Rayer, P., Matricardi, M., Geer, A., Lupu, C., Brunel, P., and Vidot, J.: RTTOV-11—Science and validation report. NWP SAF Tech. Rep., 62 pp., 2013.

Shu, C. W. and Osher, S.: Efficient implementation of essentially non-oscillatory shock-capturing schemes. Journal of Computational Physics 77(2): 439−471, https://doi.org/10.1016/0021-9991(88)90177-5, 1988.

Sitnikov, N. M., Yushkov, V. A., Afchine, A. A., Korshunov, L. I., Astakhov, V. I., Elanovskii, A. E., Kraemer, M., Mangold, A., Schiller, C., and Ravegnani, F.: The FLASH instrument for water vapor measurements on board the high-altitude airplane. Instrum. Exp. Tech., 50, 113−121, https://doi.org/10.1134/S0020441207010174, 2007.

Smith, J. B., Wilmouth, D. M., Bedka, K. M., Bowman, K. P., Homeyer, C. R., Dykema, J. A., Sargent, M.

638   R., Clapp, C. E., Leroy, S. S., Sayres, D. S., Dean-Day, J. M., Bui, T. P., and Anderson, J. G.: A case

639   study of convectively sourced water vapor observed in the overworld stratosphere over the United

640   States. J. Geophys. Res, 122, 9529−9554, https://doi.org/10.1002/2017JD026831, 2017.

641   Tissier, A.-S. and Legras, B.: Convective sources of trajectories traversing the tropical tropopause layer.

642   Atmos. Chem. Phys., 16, 3383−3398, https://doi.org/10.5194/acp-16-3383-2016, 2016.

643   Tzella, A. and Legras, B.: A Lagrangian particle dispersion model FLEXPART version 6.2. Atmos. Chem.

644   Phys., 5, 2461−2474, https://doi.org/10.5194/acp-5-2461-2005, 2005.

645   Winker, D. M., Vaughan, M. A., Omar, A., Hu, Y., Powell, K. A., Liu, Z., Hunt, W. H., and Young, S. A.:

646   Overview of the CALIPSO mission and CALIOP data processing algorithms. J. Atmos. Oceanic

647   Technol., 26, 2310–2323, https://doi.org/10.1175/2009JTECHA1281.1, 2009.

648   WMO: Definition of the tropopause, WMO Bull., 6, 136, 1957.

649   Wright, J. S., Fu, R., Fueglistaler, S., Liu, Y. S., and Zhang, Y.: The influence of summertime convection over

650   Southeast Asia on water vapor in the tropical stratosphere. J. Geophys. Res., 116, D12302,

651   https://doi.org/10.1029/2010JD015416, 2011.

652   Zöger, M., Afchine, A., Eicke, N., Gerhards, M.-T., Klein, E., McKenna, D., Mörschel, U., Schmidt, U., Tan,

653   V., Tuitjer, F., Woyke, T., and Schiller, C.: Fast in situ stratospheric hygrometers: A new family of

654   balloon-borne and airborne Lyman-photofragment fluorescence hygrometers, J. Geophys. Res., 104,

655   1807−1816, https://doi.org/10.1029/1998JD100025, 1999.

656
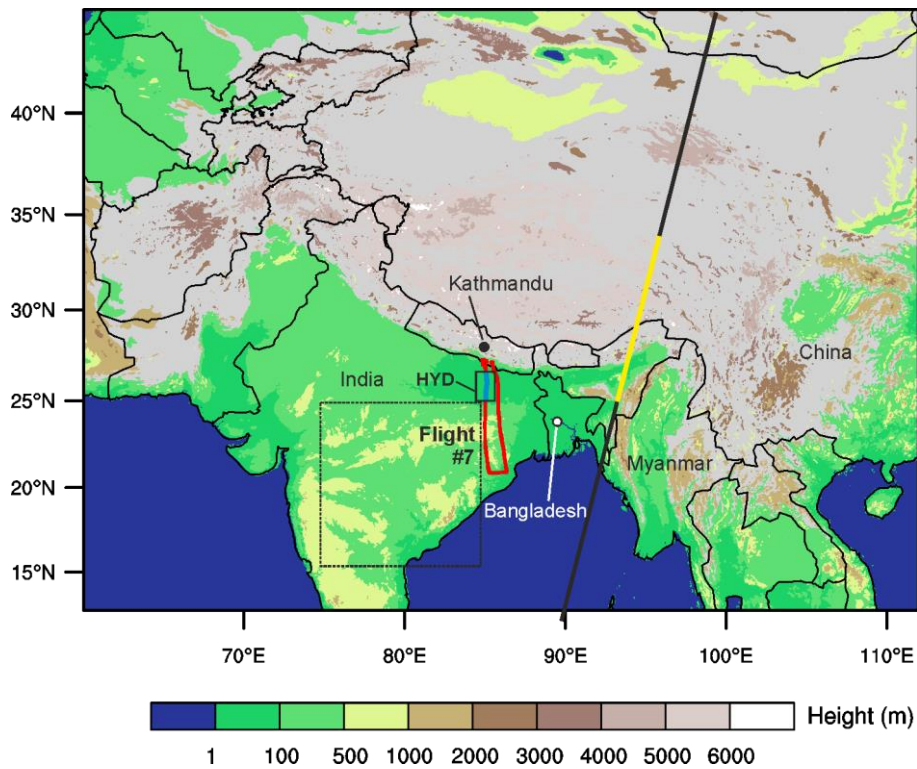
657

658 **Figure 1.** Topography and domain considered in the Meso-NH numerical simulation with a resolution of 2.5 km. The trajectory of

659 the Geophysica flight #7 to the south of Kathmandu is shown by the red solid line, while the pathway of moist patch (25−26.5°N) is

660 depicted by the blue line. A black box 'HYD' is a model domain considered in comparison with aircraft measurement. Another box

661 with dashed line is a model domain used to calculate the background water vapour at 06:00 UTC on 8 August 2017. The track of

662 CALIOP around 20:00 UTC on 7 August 2017 is shown by the black solid line while its track between 25 and 33°N is highlighted in

663 yellow.

664
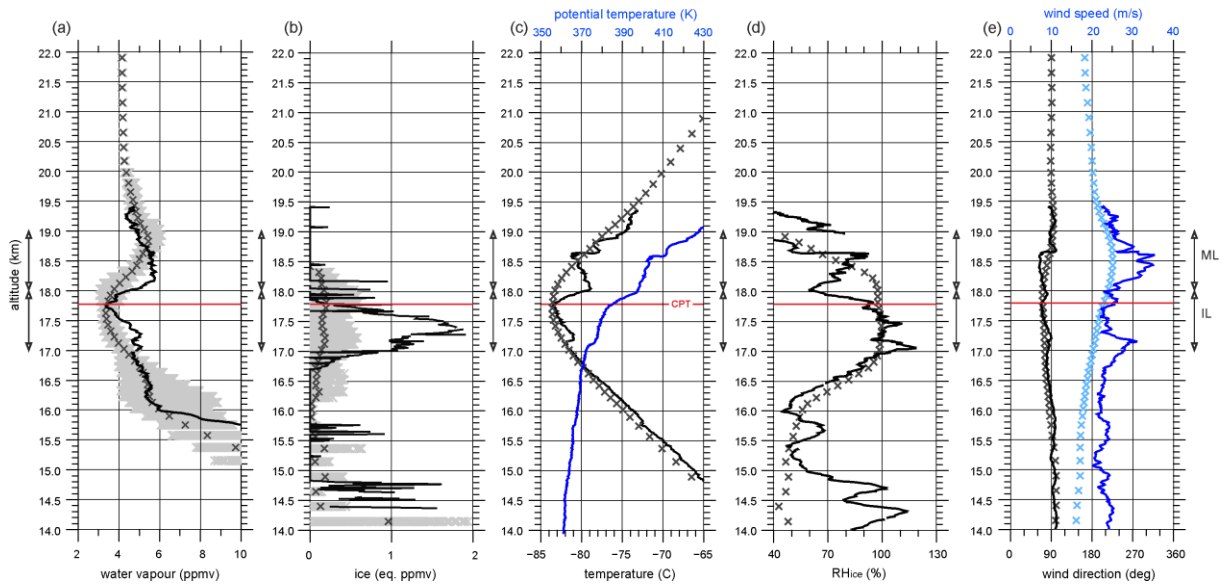
Figure 2. Vertical profiles of (a) water vapour (ppmv), (b) ice (eq. ppmv), (c) temperature (°C) and potential temperature (K), (d) relative humidity respect to ice (RH$_{ice}$, %), and (e) wind direction (degree) and speed (m s^{-1}). In (a)−(e), the measured values along the blue-coloured track between 25−26.5°N (shown in Fig. 1) from 06:20 to 06:48 UTC on 8 August 2017 are shown as solid line, while the domain averaged values in the region 'HYD' (25−26.5°N, 85−85.5°E, shown in Fig. 1) from the Meso-NH simulation at 06:00 UTC on the same day are shown as cross marks. In (a)–(e), the level of cold point tropopause (CPT) is indicated by a red line. In (a)−(b), all the values from Meso-NH within the 'HYD' is displayed by grey cross marks. The layers of ML and IL are marked by arrows.

673
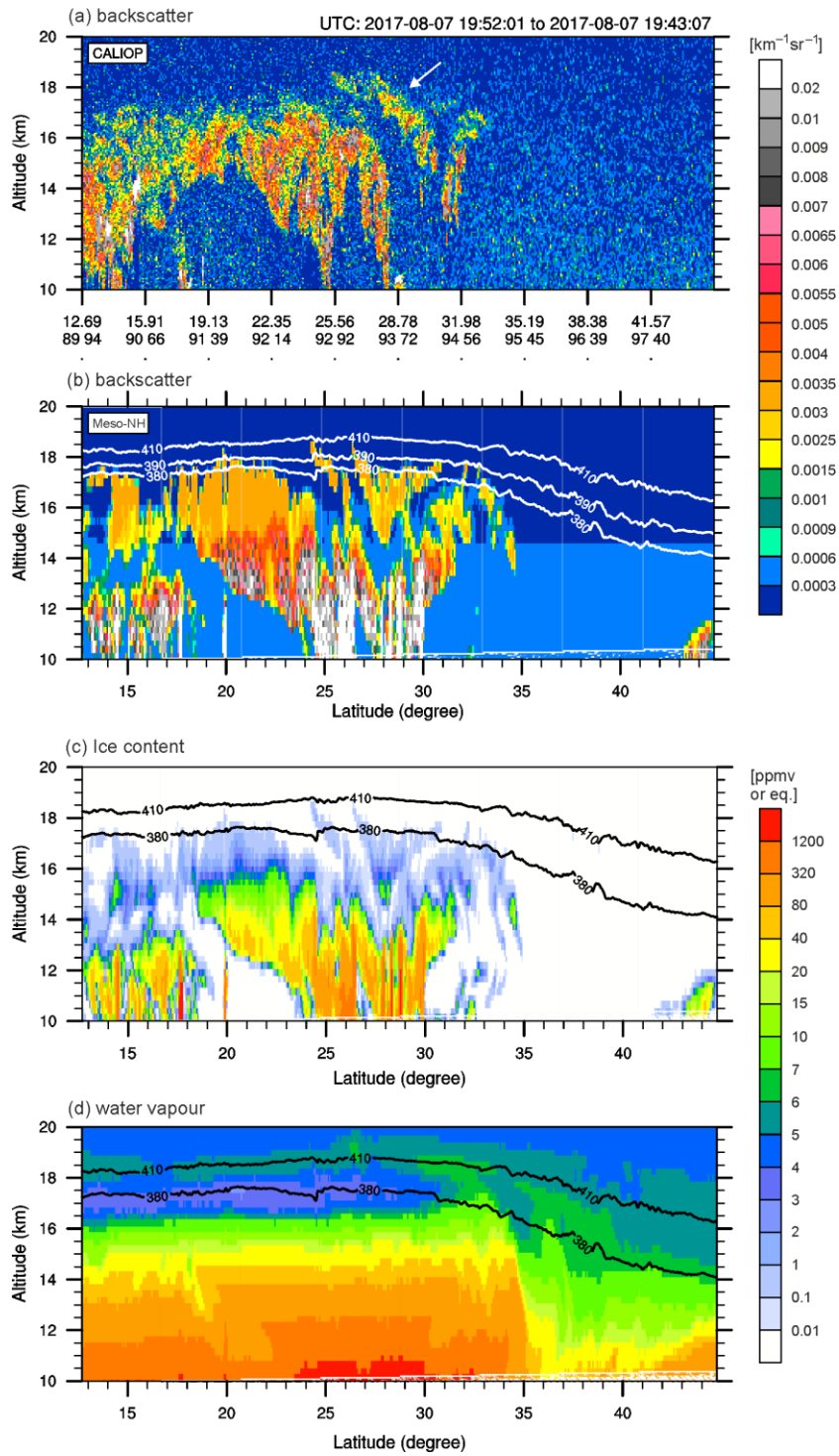
Figure 3. Backscatters at 532 nm (a) measured by CALIOP around 20:00 UTC and (b) retrieved by the Meso-NH simulation, and (c)

ice content (eq. ppmv) and (d) water vapour (ppmv) produced by the Meso-NH simulation along the CALIOP track (marked by solid

line in Fig. 1) at 20:00 UTC on 7 August 2017.

677
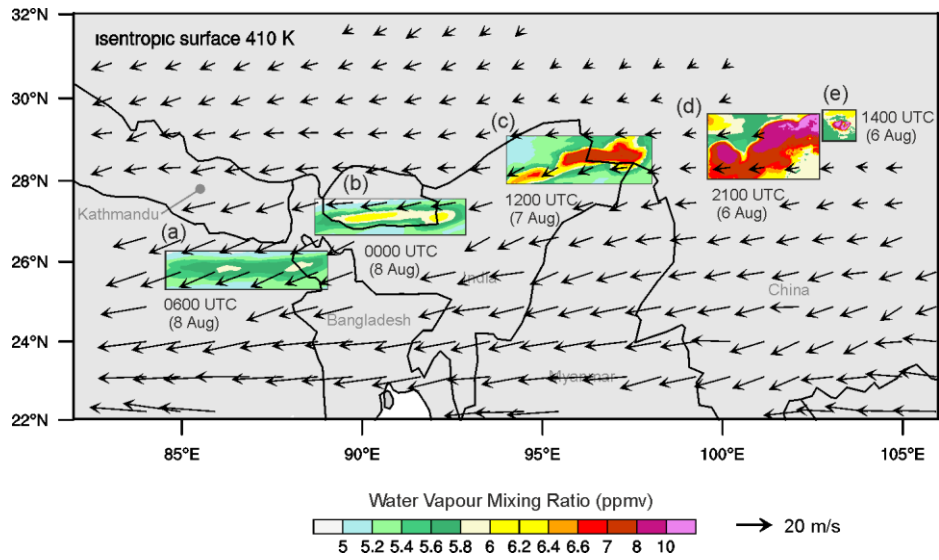
Figure 4. Target moist patch. Horizontal distribution of water vapour mixing ratio at 410 K isentropic altitude at (a) 06:00 UTC, and (b) 00:00 UTC on 8 August, (c) 12:00 UTC on 7 August, (d) 21:00 UTC and (e) 14:00 UTC on 6 August 2017. The horizontal wind at the altitude of 19 km (about 410 K isentrope) at 06:00 UTC on 8 August is displayed by vectors.

682
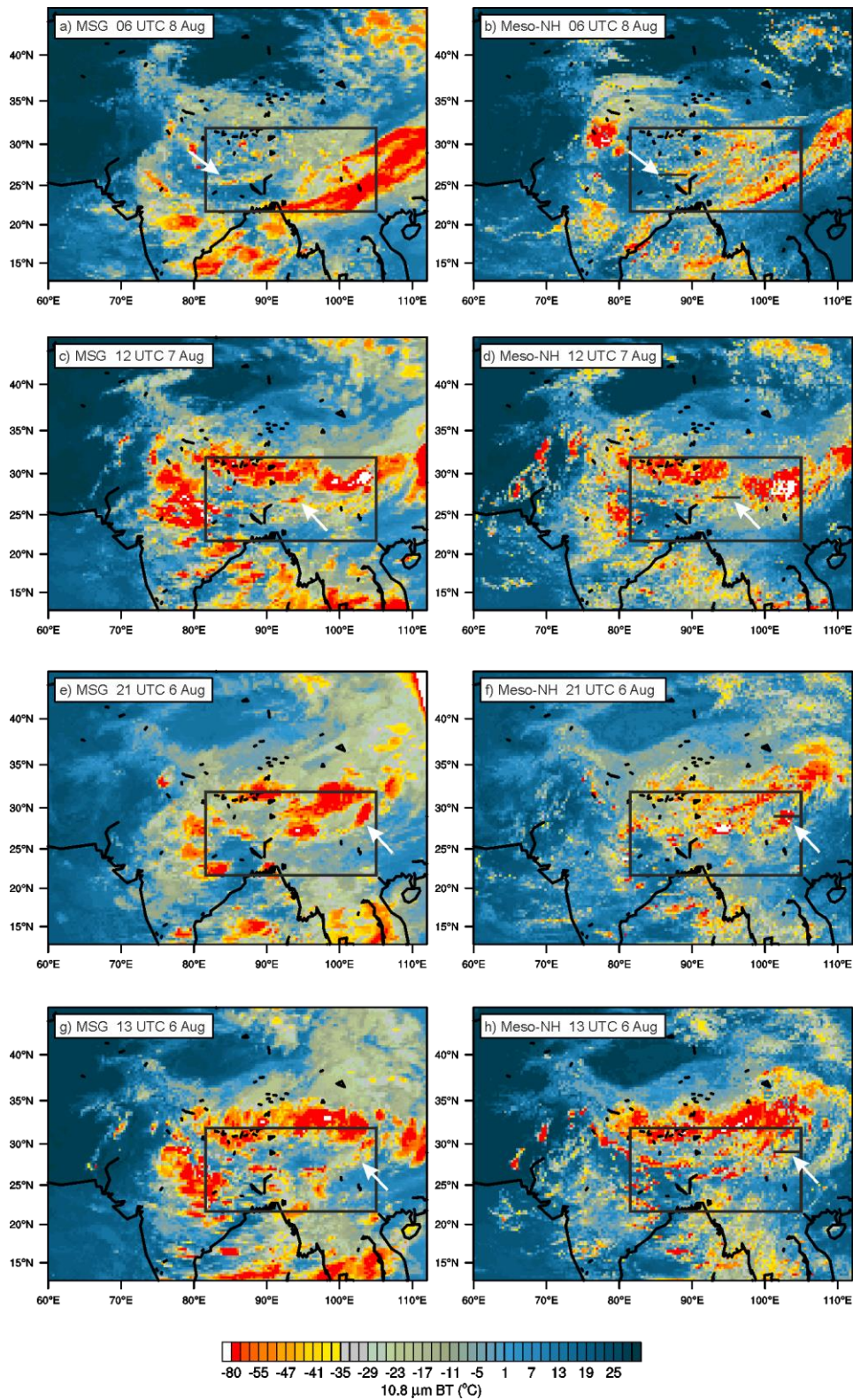
Figure 5. BT 10.8 μm obtained from SEVIRI/MSG (left) and Meso-NH (right) at (a)−(b) 06:00 UTC on 8 August, (c)−(d) 12:00

UTC on 7 August, (e)−(f) 21:00 UTC, and (f)−(h) 13:00 UTC on 6 August 2017. The domain used in Figure 4 is marked by a box in

each panel, while the location of vertical cross-sections used in Figures 6−9 is marked by a black solid line in the right panels. The

location of hydration patch is depicted by the white arrows.
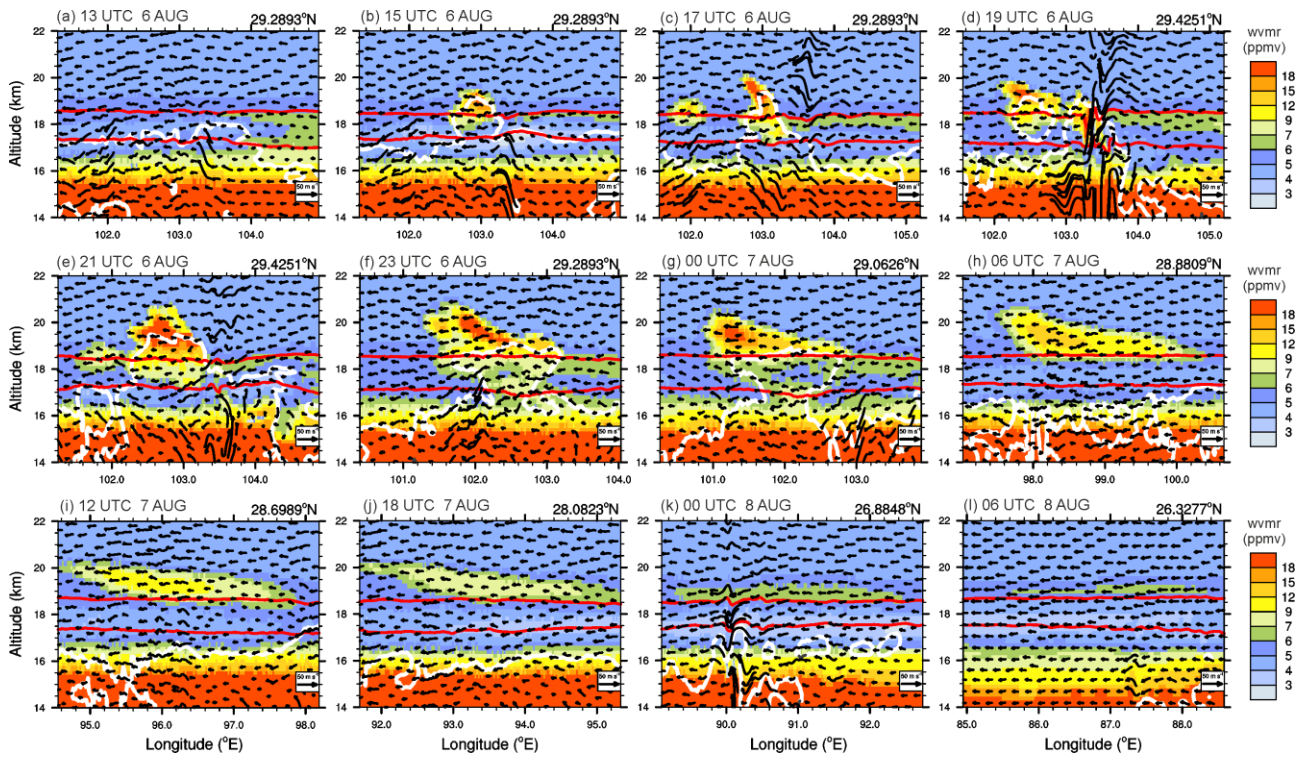
Figure 6. Vertical cross-sections of water vapour mixing ratio (shading) and wind (vectors) (a) 13:00 UTC, (b) 15:00 UTC, (c) 17:00 UTC, (d) 19:00 UTC, (e) 21:00 UTC, (f) 23:00 UTC on 6 August 2017, (g) 00:00 UTC, (h) 06:00 UTC, (i) 12:00 UTC, (j) 18:00 UTC on 7 August 2017, and (k) 00:00 UTC and (l) 06:00 UTC on 8 August 2017. The isentropic altitudes of 380 and 410 K are depicted by the red lines. The latitude (°N) of west-east oriented cross-section line is indicated at the upper right of each panel. The cloud boundary (mixing ratio of ice content of 10 mg kg^{-1}) is contoured by the white solid line.
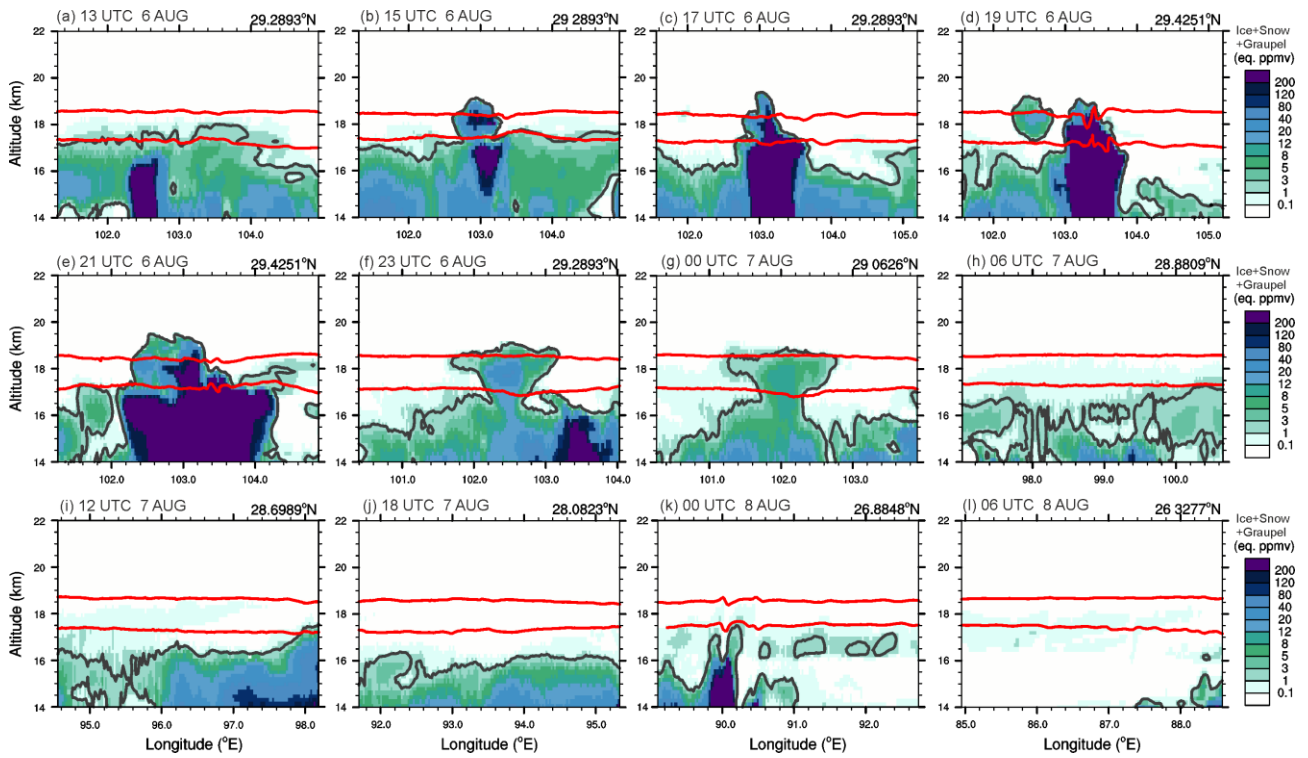
Figure 7. Same as Fig. 6 but for the ice content. The isentropic altitudes of 380 and 410 K are depicted by the red lines.
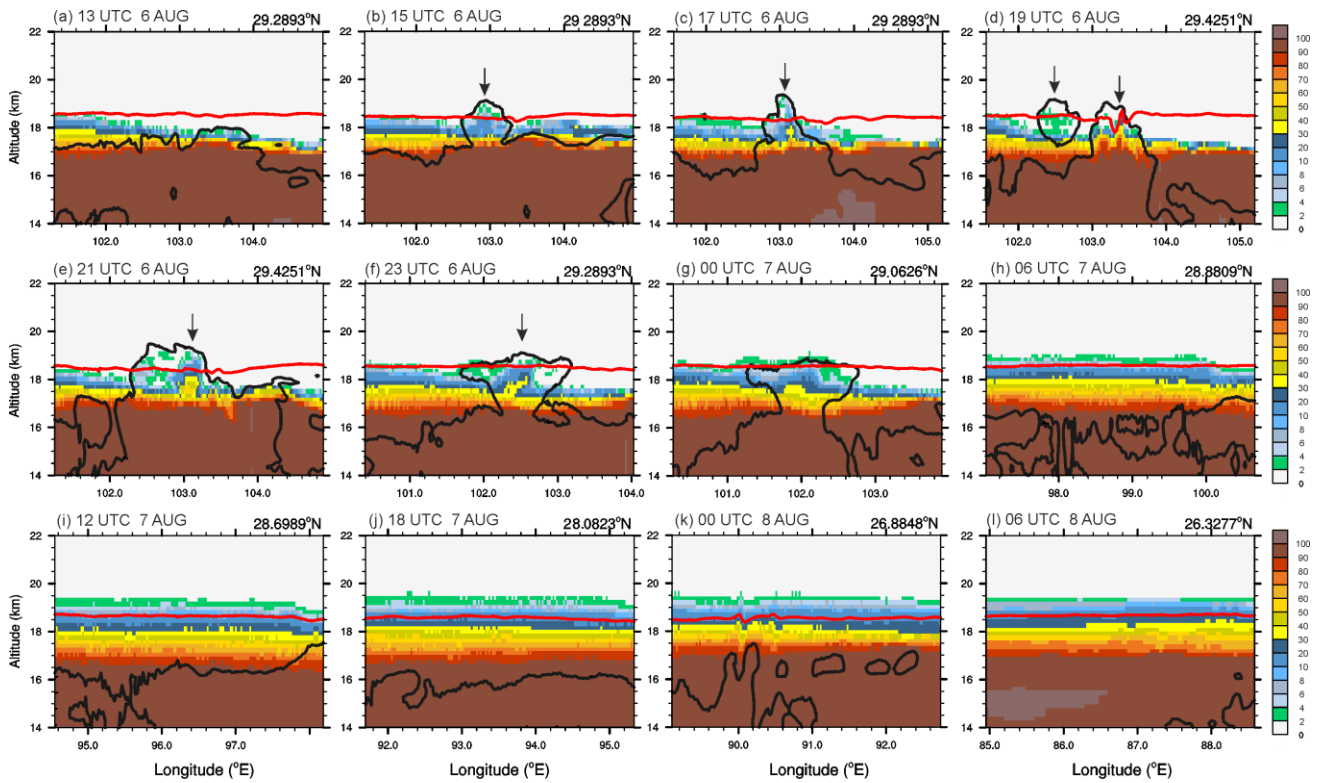
Figure 8. Same as Fig. 6 but for the tracer (%). The isentropic altitude of 410 K is depicted by the red line. The changes of the

tropospheric tracer by convective overshoots is marked by downward arrows.
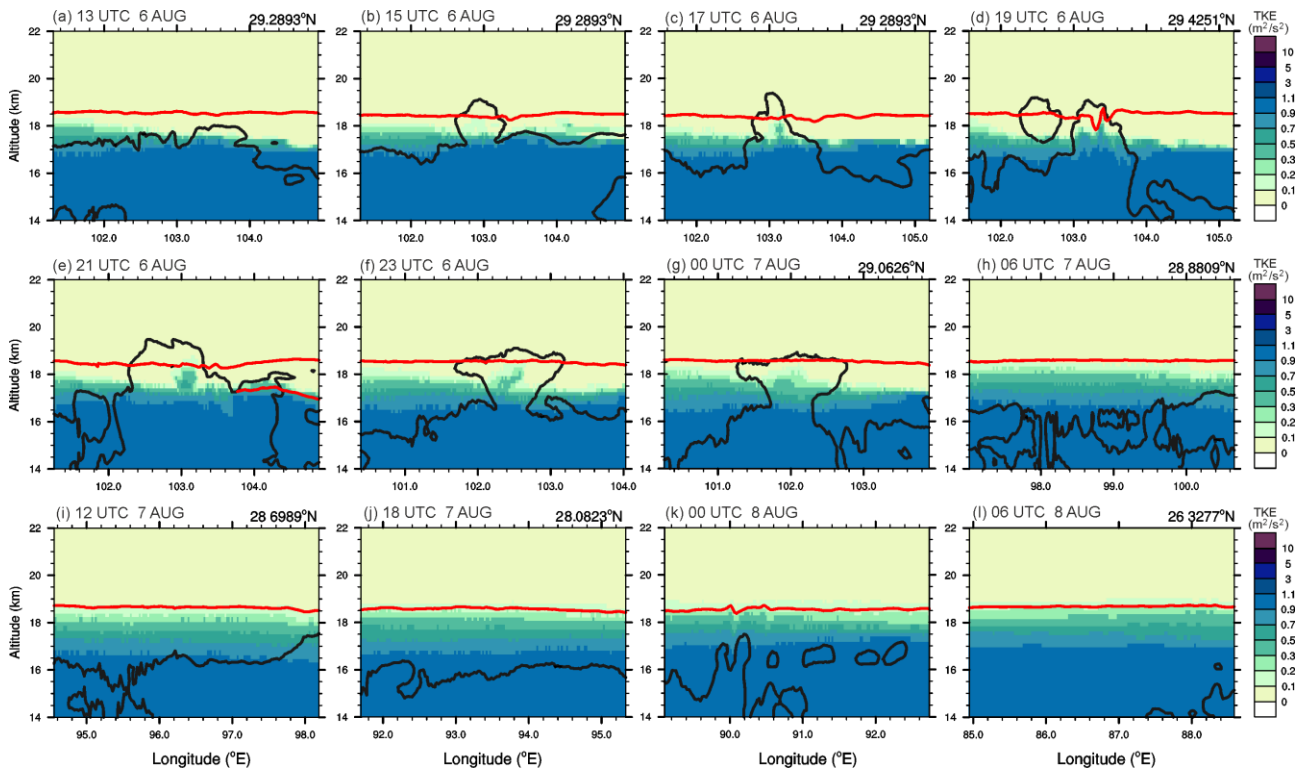
Figure 9. Same as Fig. 6 but for the TKE. The isentropic altitude of 410 K is depicted by the red line.
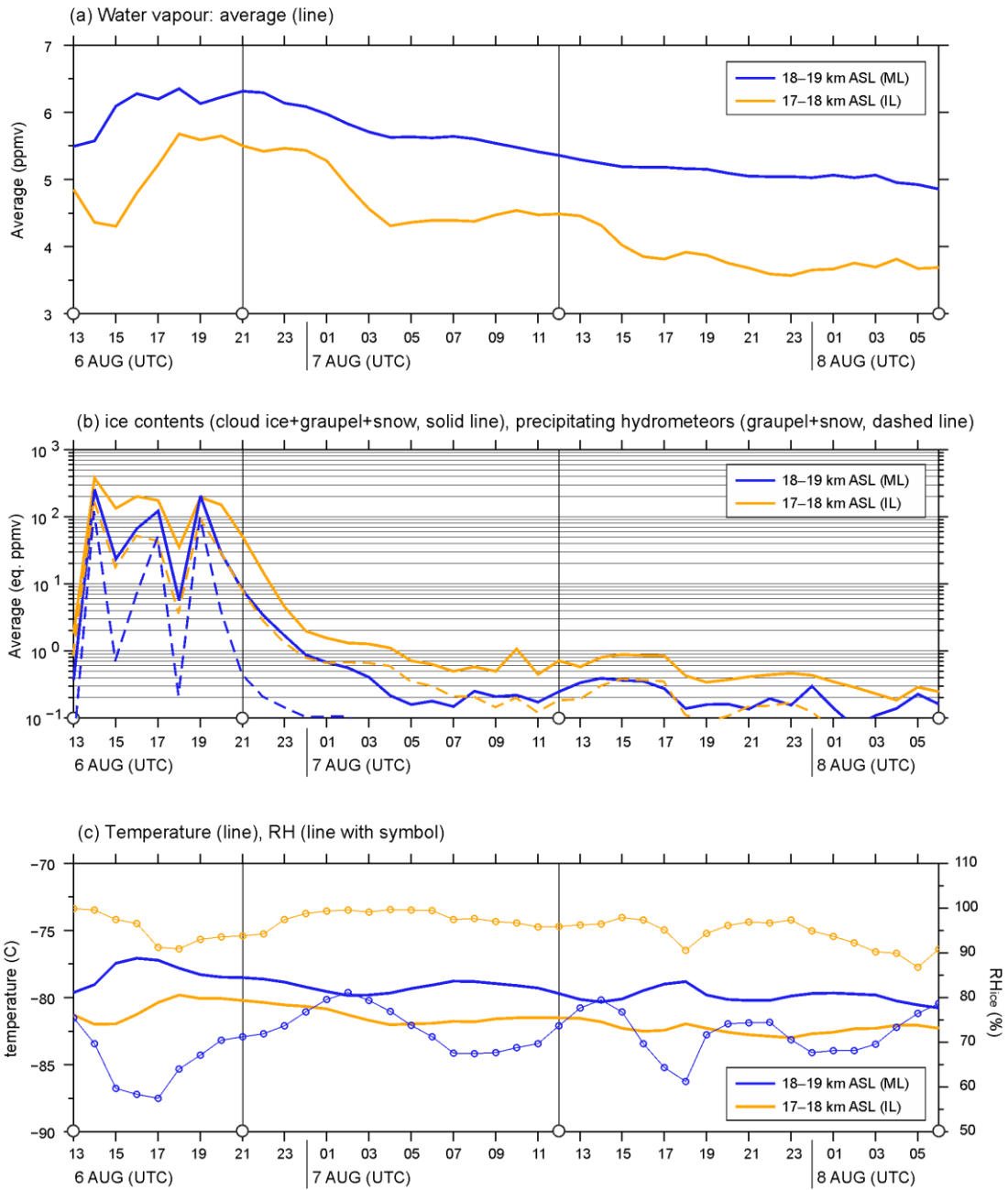
Figure 10. Hourly evolution of (a) averaged water vapour (line), (b) averaged ice content (solid line, sum of ice, graupel, and snow) and the precipitating hydrometeor (dashed line, sum of graupel and snow), and (c) averaged temperature (line) and relative humidity (RH$_{ice}$, thin line with circle) in the altitudes of 17−18 km (yellow lines) and 18−19 km (blue lines) ASL from 13:00 UTC on 6 August to 06:00 UTC on 8 August 2017. The four analysis times are marked by open circles on the x-axis. Average and maximum values are calculated in ML and IL.
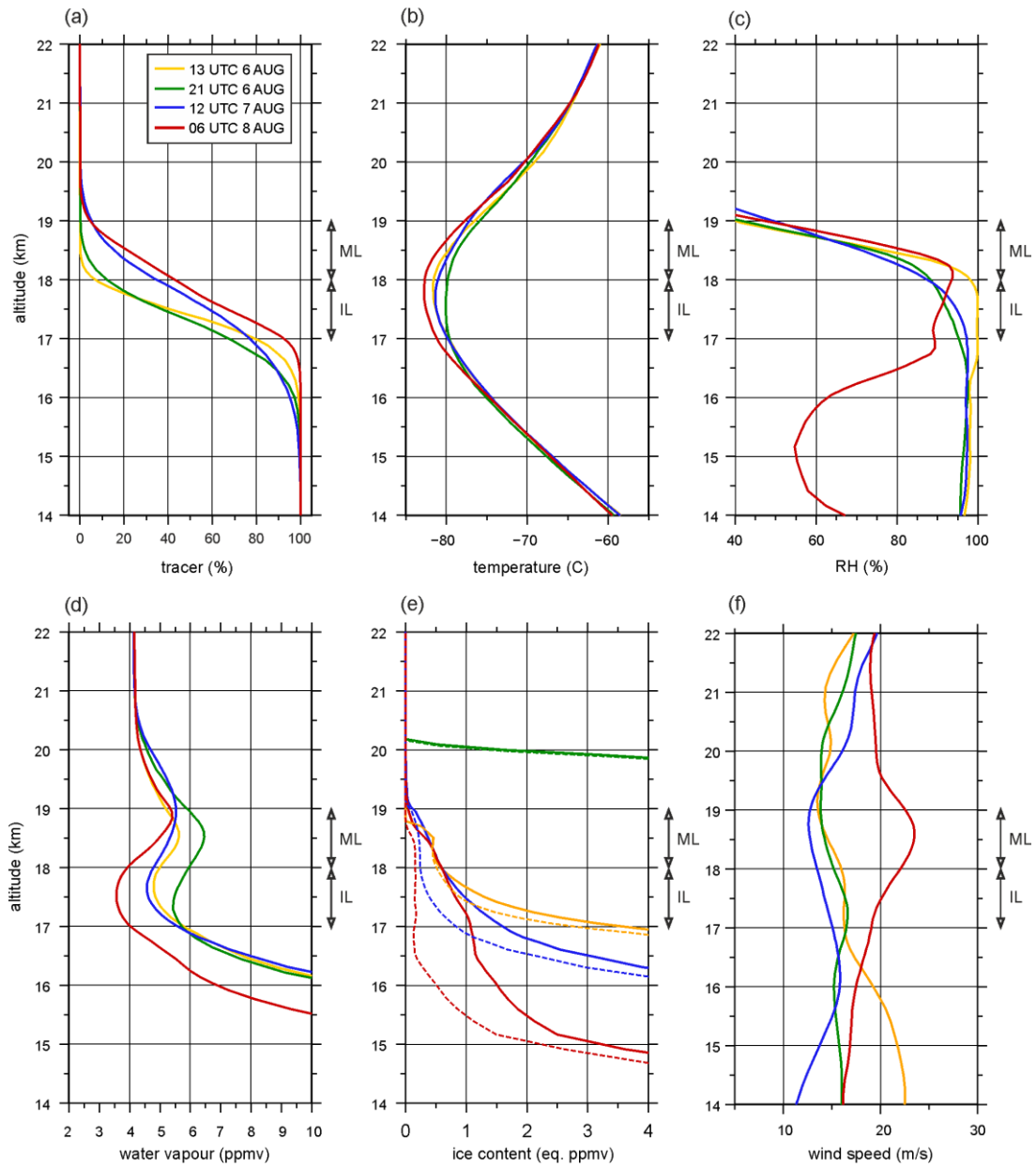
Figure 11. Vertical profiles of (a) tracer (%), (b) temperature (°C), (c) relative humidity (%), mixing ratios of (d) water vapour (ppmv), (e) ice content (eq. ppmv), and (f) wind speed (m s⁻¹) across the hydration patch along the trajectory at 13:00 UTC (yellow line), 21:00 UTC (green line) on 6 August, 12:00 UTC on 7 August (blue line), and 06:00 UTC (red line) on 8 August 2017. The layers of ML and IL are marked by arrows. In (e), the ice content is depicted by solid lines, while the cloud ice are shown by dashed lines.

721
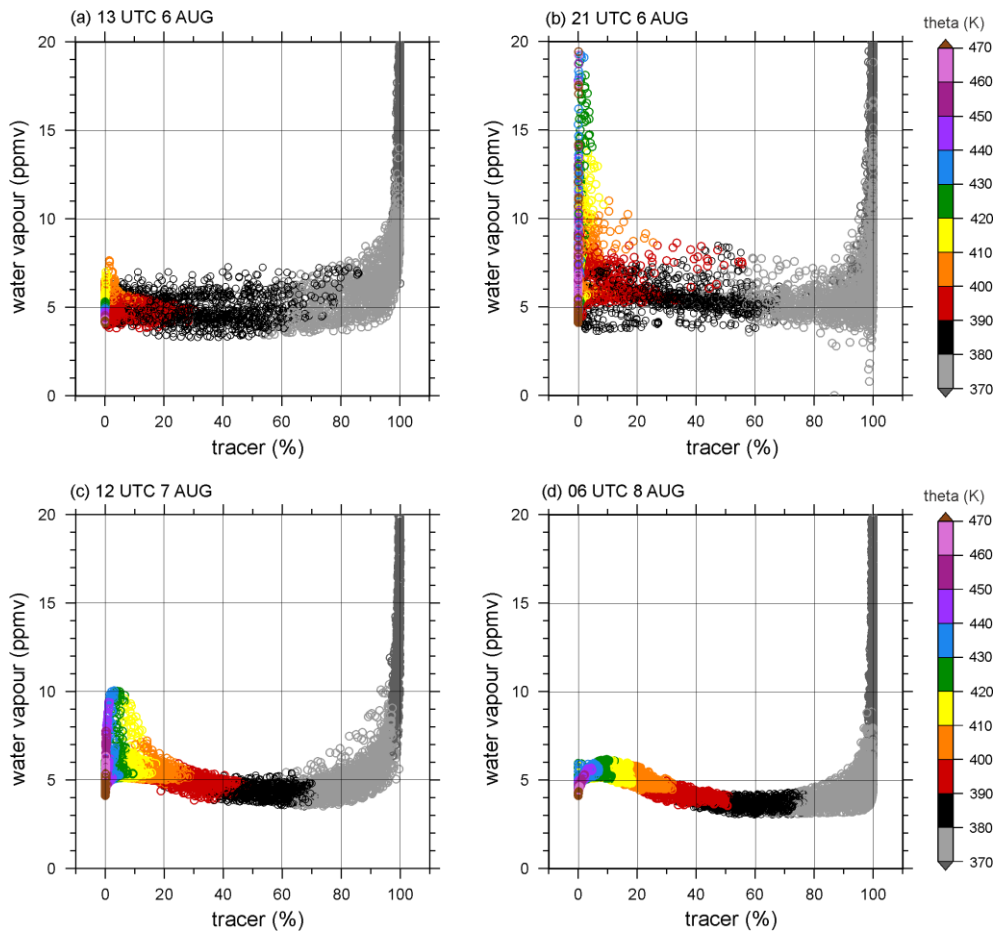
722 **Figure 12.** Mixing diagram using tropospheric tracer (%) and water vapour (ppmv) across the hydration patch in the altitudes

723 between 14 and 22 km ASL along the trajectory at (a) 13:00 UTC on 6 August, (b) 21:00 UTC on 6 August, (c) 12:00 UTC on 7

724 August, and (d) 06:00 UTC on 8 August 2017. The potential temperature (K) is shown with colour shading.
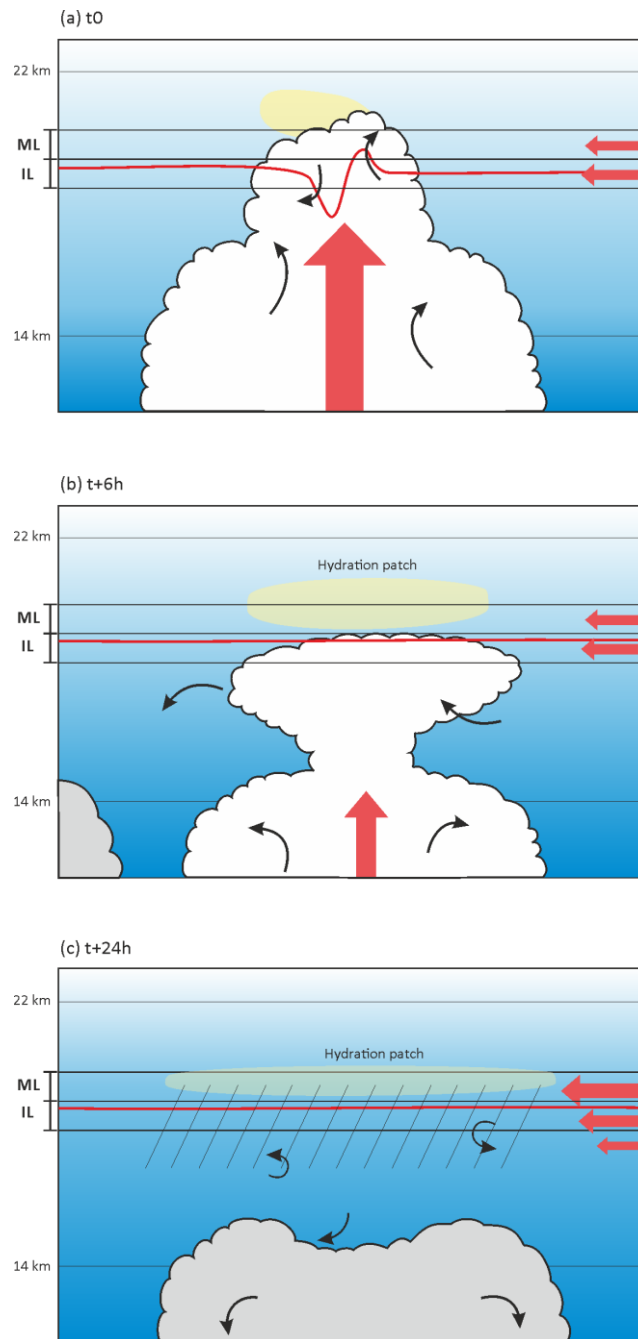
Figure 13. Schematic illustration summarising the hydration process in the TTL during flight #7 of the StratoClim 2017 field campaign. (a) Mixing of the overshoots with the stratospheric air, (b) and (c) turbulent mixing of the hydration patch with the tropospheric air by vertical wind shear. The bottom and top of the TTL, 14 and 22 km, and the moist layer (ML) and ice layer (IL) are represented by the black solid line, and the 410 K isentropic altitude is represented by the red solid line. The main force in the TTL is marked by bold red arrows, while the turbulent eddies in/around the developed and weakened overshoots are described by black arrows. The overreaching water vapour above the cloud top level is indicated by a yellow ellipsoid in (a). The hydration patch is yellow-encapsulated in (a) and (b), and the layer of dehydration by turbulent diffusion and water vapour deposition followed by ice sedimentation is hatched in (c). The blue shades illustrate the concentration of tropospheric air, showing the increased tropospheric air in the TTL by the turbulent mixing in (b) and (c).